Impaired Kupffer Cell Self-Renewal Alters the Liver Response to Lipid Overload during Non-alcoholic Steatohepatitis

Sophie Tran, Ines Baba, Lucie Poupel, Sébastien Dussaud, Martine Moreau, Adélaïde Gélineau, Geneviève Marcelin, Elissa Magréau-Davy, Melissa Ouhachi, Philippe Lesnik, et al.

Impaired Kupffer cell self-renewal alters the liver response to lipid overload during non-alcoholic steatohepatitis.

Sophie Tran[1#], Ines Baba[1#], Lucie Poupel[1], Sébastien Dussaud[1], Martine Moreau[1], Adélaïde Gélineau[1], Geneviève Marcelin[2], Elissa Magréau-Davy[1], Melissa Ouhachi[1], Philippe Lesnik[1], Alexandre Boissonnas[3], Wilfried Le Goff[1], Björn E. Clausen[4], Laurent Yvan-Charvet[5], Florian Sennlaub[6], Thierry Huby[1], Emmanuel L. Gautier[1,7,*].

[1] Institut National de la Santé et de la Recherche Médicale (Inserm, UMR_S 1166), Sorbonne Université, Hôpital de la Pitié-Salpêtrière, Paris, France.
[2] Institut National de la Santé et de la Recherche Médicale (Inserm, UMR_S 1269), Sorbonne Université, Hôpital de la Pitié-Salpêtrière, Paris, France.
[3] Institut National de la Santé et de la Recherche Médicale (Inserm, UMR1135), Sorbonne Université, Centre National de la Recherche Scientifique (CNRS, ERL8255), Centre d'Immunologie et des Maladies Infectieuses CIMI, Paris, France.
[4] Institute for Molecular Medicine, University Medical Center of the Johannes Gutenberg-University Mainz, Mainz, Germany.
[5] Institut National de la Santé et de la Recherche Médicale (Inserm, U1065), Université Côte d'Azur, Centre Méditerranéen de Médecine Moléculaire (C3M), Atip-Avenir, Fédération Hospitalo-Universitaire (FHU) Oncoage, Nice, France.
[6] Institut de la Vision, Sorbonne Université, Institut National de la Santé et de la Recherche Médicale (Inserm), Centre National de la Recherche Scientifique (CNRS), Paris, France.
[7] Lead Contact
[*] Corresponding author
[#] These authors contributed equally to this work

Running title: Kupffer cell diversity in NASH.

Subject terms:
Macrophages
Kupffer cells
Monocytes
Steatohepatitis

Address correspondence to:
Lead Contact
Dr. Emmanuel L. Gautier
INSERM UMR_S 1166
Sorbonne Université
Faculté de Médecine
Hôpital de la Pitié-Salpêtrière
Paris, France
emmanuel-laurent.gautier@inserm.fr

SUMMARY

Kupffer cells (KCs) are liver-resident macrophages that self-renew by proliferation in the adult independently from monocytes. However, how they are maintained during non-alcoholic steatohepatitis (NASH) remains ill-defined. We found that a fraction of KCs derived from Ly-6C$^+$ monocytes during NASH, underlying impaired KCs self-renewal. Monocyte-derived KCs (MoKCs) gradually seeded the KC pool as disease progressed in a response to embryo-derived KC (EmKC) death. Those MoKCs were partly immature and exhibited a pro-inflammatory status compared to EmKCs. Yet, they engrafted the KC pool for long-term as they remained following disease regression while acquiring mature EmKC markers. While KCs as a whole favored hepatic triglyceride storage during NASH, EmKCs promoted it more efficiently than MoKCs and the latter exacerbated liver damage, highlighting functional differences among KCs with different origins. Overall, our data reveal that KC homeostasis is impaired during NASH, altering the liver response to lipids as well as KC ontogeny.

INTRODUCTION

Tissue-resident macrophages are essential to preserve tissue homeostasis (Wynn et al., 2013). Kupffer cells (KCs), the tissue-resident macrophages inhabiting the liver, are located in the hepatic sinusoids where they sample both the portal and arterial blood circulation. The role of KCs in several aspects of the immune response (Jenne and Kubes, 2013), in particular the response to blood-borne pathogens (Surewaard et al., 2016; Zeng et al., 2016) is well appreciated, but many of their accessory functions remain to be uncovered.

KCs develop embryonically (Gomez Perdiguero et al., 2015; Hoeffel et al., 2015) and are maintained independently from circulating monocytes in the healthy adult, relying on local proliferation to self-renew and sustain in the long-term. However, when depleted through high-dose irradiation (Beattie et al., 2016) or diphteria toxin-mediated killing (Scott et al., 2016), embryo-derived KCs (EmKCs) are replaced by monocyte-derived KCs (MoKCs). In addition, KC-specific deletion of the transcription factors ZEB2 and LXRα, which are necessary for KC self-maintenance (Mass et al., 2016; Scott et al., 2018), equally lead to the generation of MoKCs filling up the empty niche. To date, whether KC maintenance is impaired during physiopathological processes is still poorly understood. Several pieces of evidence suggest that monocyte-derived KCs (MoKCs) are generated during *Listeria monocytogenes* infection (Blériot et al., 2015) or in mouse models where massive red blood cell lysis occurs (Theurl et al., 2016), but such MoKCs might not be maintained in the long-term (Theurl et al., 2016). In addition, whether MoKCs are commonly observable in other pathological states, especially in chronic liver diseases, remains elusive.

The most prominent form of liver disease in the western world, affecting approximately one third of the population (Hardy et al., 2016), is nonalcoholic fatty liver disease (NAFLD). Its incidence keeps growing due to its close association with obesity, type 2 diabetes and the metabolic syndrome (Hardy et al., 2016). NAFLD includes a spectrum of liver disorders ranging from nonalcoholic fatty liver (NAFL), more commonly termed steatosis, to nonalcoholic steatohepatitis (NASH). NASH, which is characterized by steatosis, inflammation, ballooning injury and varying degrees of fibrosis (Hardy et al., 2016), represents the first critical stage of NAFLD. Macrophages are believed to be essential for controlling the inflammatory process during NASH (Krenkel and Tacke, 2017). Indeed, whole body monocyte and macrophage depletion attenuates the progression towards NASH in animal models (Huang et al., 2010; Reid et al., 2016). However, it is unclear whether those effects are attributable to inflammatory monocyte-derived macrophages (MoDMacs) or KCs. More generally, KC biology in NASH remains poorly investigated, especially due to the lack of validated strategies to discriminate, isolate and therefore study KCs.

Here we set out to determine whether KC self-renewal is disturbed in the context of NASH. Our findings reveal steatohepatitis has a major and long-lasting impact on KCs ability to self-maintain that in turn alters the liver response to lipid overload.

RESULTS

CLEC2 discriminates KCs from MoDMacs in NASH.

In order to specifically distinguish KCs by flow cytometry, we looked for surface markers discriminating KCs from the inflammatory MoDMacs found in inflamed livers. We and others have previously reported considerable heterogeneity in the transcriptional profile among different tissue-resident macrophages (Gautier et al., 2012a; Lavin et al., 2014). Data-mining of published tissue-resident macrophage transcriptome analysis (Gautier et al., 2012a; Lavin et al., 2014), including KCs, revealed several markers selectively expressed by KCs but not MoDMacs (Supplemental Figures 1A and 1B). In particular, CLEC2 (encoded by *Clec1b*), CD207 (also known as Langerin), VSIG4 (also known as CRIg) and TIMD4 (also known as TIM-4) were either very selectively and/or strongly expressed by KCs. Flow cytometry analysis of KCs, defined as $CD64^{+}$ $F4/80^{hi}$ cells (Figure 1A), in the healthy liver revealed that they homogeneously expressed those markers, with particularly high expression of CLEC2 (Figure 1B). We also validated that all $CLEC2^{hi}$ leukocytes in the naïve liver were indeed KCs with their typical $F4/80^{hi}$ expression profile (Figure 1C). We next asked whether CLEC2 would help to discriminate KCs from MoDMacs during NASH. We chose the model of methionine and choline deficient (MCD) diet-induced NASH, which recapitulates the ultrastructural changes observed in human patients (Machado et al., 2015), thus closely resembling human NASH histological features. MCD diet feeding of wild-type mice for 6 weeks induced liver dysfunction. This was characterized by increased plasma alanine aminotransferase (ALT) activity (Figure 1D) and elevated hepatic triglyceride content (Figure 1E), mostly as macrovesicular droplets into hepatocytes (Supplemental Figure 1C), in MCD-fed animals. To discriminate KCs from MoDMacs, we first gated on KCs defined as $CD11b^{lo}$ $CLEC2^{hi}$ cells (Figure 1F). Among the remaining cells, we identified $CLEC2^{-}$ $CD11b^{+}$ $CD64^{+}$ MoDMacs that appeared upon MCD diet feeding (Figure 1F). Finally, Ly-$6C^{+}$ $CD11b^{+}$ monocytes and Ly-$6C^{int}$ $CD11b^{hi}$ neutrophils were identified in the $CLEC2^{-}$ $CD11b^{+}$ $CD64^{-}$ fraction (Figure 1F). Then, we observed that KCs accumulated intracellular lipids upon MCD feeding (Figure 1G), while their proliferative status remained unchanged (Figure 1H). Intracellular lipid content in MoDMacs also increased in MCD-fed animals when they were compared to the scarce cells we found in that gate in chow-fed controls (Bodipy MFI of 9868±944 in the MCD conditions versus 3597±1048 in controls, $P<0.01$), but it was markedly lower than in KCs. Overall, we found that KC numbers during NASH remained similar to the control condition while MoDMacs and Ly-$6C^{+}$ monocyte numbers, as well as neutrophils (data not shown), drastically increased (Figure 1I). Of note, we also evaluated the gating strategy presented above in pre-NASH models of steatosis such as *Ob/Ob* mice and high-fat diet (HFD)-fed mice and could confirm the coexistence of MoDMacs and KCs in these models (Supplemental Figure 1D-I). Next, we challenged *Ccr2*$^{-/-}$ mice, characterized by low circulating Ly-$6C^{hi}$ monocytes, with the MCD diet in order to ascertain the monocytic origin of MoDMacs. As expected, liver Ly-$6C^{hi}$ monocyte counts and MoDMac numbers were extremely low in *Ccr2*$^{-/-}$ mice (Figures 1J and 1K). In addition to MoDMacs, we noticed that KC counts decreased by half in *Ccr2*$^{-/-}$ animals (Figure 1K). Such decrease in KCs was not observed in condition of steatosis when *Ccr2*$^{-/-}$ were challenged with a HFD (Supplemental Figure 1I), suggesting NASH but not steatosis altered KCs homeostasis. These observations suggest that, contrary to homeostasis, circulating monocytes contribute to the KC pool during NASH.

MoKCs are generated during NASH to maintain the KC pool.

To establish the monocytic origin of KCs during NASH, we aimed to track Ly-6C^{hi} monocytes fate. We thus developed bone marrow (BM) chimeras using CD45.2^{+} *Ccr2*$^{-/-}$ recipients submitted to low dose irradiation (3 Gy) and transplanted with 5-10 x 10^{6} BM cells from congenic CD45.1^{+} donors (Figure 2A). We reasoned that such a mild irradiation regimen would be sufficient to favor the engraftment of donor cells that will generate CCR2-sufficient monocytes able to enter the bloodstream, while it would spare radioresistant KCs. To validate our strategy, we determined the chimerism of circulating monocytes 2 weeks after transplantation and found that more than 80% of Ly-6C^{hi} and Ly-6C^{lo} monocytes were derived from CD45.1^{+} donor cells as expected (Figures 2B and 2C). At this time point, approximately 30% of neutrophils and B cells, but less than 2% of T cells, were CD45.1^{+} (Figure 2C). Six weeks after transplantation, the chimerism observed in monocytes, neutrophils and B cells was comparable to the 2-week time point (Figure 2D). Therefore, these chimeras should allow us to track the fate of monocytes during NASH by determining the fraction of CD45.1^{+} cells in our populations of interest.

These chimeras were put on a standard chow or MCD diet for 6 weeks and hepatic macrophage subsets chimerism was assessed. As expected, a minor fraction of KCs (<2%) were CD45.1^{+} under chow diet, reflecting their radioresistance (Figures 2E and 2F). By contrast, almost all MoDMacs (>90% CD45.1^{+}) were derived from monocytes (Figure 2E and 2F). Next, in line with our findings above (Figure 1K), we observed that ~40% of KCs were CD45.1^{+} and thus derived from monocytes in the NASH condition (Figure 2E and 2F). The fraction of those MoKCs positively correlated with the abundance of MoDMacs (Figure 2G), suggesting that increased inflammation favored MoKCs generation. In addition, we evaluated whether the impact of the MCD diet was specific to KCs, and confirmed that monocytes did not contribute to the pool of radioresistant alveolar macrophages (Figure 2H). Similar conclusions were drawn when eCFP^{+} donor cells were used for the transplantation of irradiated *Ccr2*$^{-/-}$ mice (Supplemental Figures 2A-D). In addition, WT recipient mice submitted to low dose irradiation and transplanted with CD45.1^{+} donor cells, which led to a chimerism of ~30% in Ly-6C^{+} monocytes, also harbored a fraction of their KCs that was derived from monocytes during NASH (Supplemental Figures 2E-F). We next set out to validate the participation of monocytes to the KC pool during NASH using an alternative approach. To this aim, we performed parabiosis experiments in which we joined CD45.2^{+} *Ccr2*$^{-/-}$ with congenic CD45.1^{+} or eCFP transgenic mice (Figure 2I). Ly-6C^{+} monocytes in CD45.2^{+} *Ccr2*$^{-/-}$ parabionts were derived to ~90% and ~85% from the CCR2-sufficient parabiont under chow and MCD diet, respectively (Figure 2J). Similar to our radiation chimeras, MoDMacs were exclusively derived from monocytes, while ~30% of KCs were monocyte-derived in parabiotic mice with NASH (Figure 2J). Again, alveolar macrophages were maintained independently from monocytes during NASH (Figure 2J).

To test whether MoKCs were generated during hepatic steatosis (NAFL), namely before NASH onset, *Ccr2*$^{-/-}$-based radiation chimeras were fed a HFD for 14 weeks (Figure 2K). This led to hepatic triglyceride storage (~50 µg/mg of liver, data not shown), but no overt inflammation as revealed by the paucity of MoDMacs found in the liver under these conditions (Supplemental Figure 1I). Still, NAFL triggered MoKC generation as ~8% of KCs were CD45.1^{+} (Figure 2L), thus far less than what we observed during NASH. This result was in agreement with the observed correlation between MoKCs and MoDMacs abundance (Figure 2G), suggesting that NAFL did not create an inflammatory environment necessitating MoKCs generation to maintain the KC pool. The similar KC numbers observed in *Ccr2*$^{-/-}$ mice and their wild-type controls upon HFD feeding further

supported this finding (Supplemental Figure 1I). Finally, *Ccr2*$^{-/-}$-based chimeras were fed an HFD with low content of dietary choline (CDA-HFD) (Figure 2M), a model recently used as an alternative to the MCD diet (Wolf et al., 2014). Four weeks of CDA-HFD feeding induced massive hepatic triglyceride accumulation (~200 µg/mg of liver, data not shown) and MoKC generation was extremely high in this context (Figure 2N). Overall, our findings suggest that the KC pool is unable to self-maintain during NASH, leading to the generation of MoKCs that sustain KC numbers.

MoKCs are maintained for long-term after NASH regression.

We next looked more in depth into MoKC generation, characteristics and long-term maintenance. Using *Ccr2*$^{-/-}$-based chimeras, we first noticed that the proportion of MoKCs among CLEC2^{+} KCs gradually increased during the progression of NASH (Figure 3A). Over the time course studied, monocyte chimerism was ~85%, meaning the real participation of MoKCs to the KC pool reached 60% by 6 weeks of MCD feeding (Supplemental Figure 2G). Next, to better characterize MoKCs, *Ccr2*$^{-/-}$-based chimeras generated as described above were fed a chow or the MCD diet. In order to evaluate the mRNA expression of the classical KC markers (*Clec4f*, *Cd163* and *Vsig4)*, EmKCs were sorted from chow-fed healthy mice and EmKCs, MoKCs and MoDMacs from mice with NASH. As expected, MoDMacs did not express these markers while EmKCs from healthy and NASH conditions similarly expressed *Clec4f*, *Cd163* and *Vsig4* (Figure 3B). By contrast, MoKCs did not express these markers as compared to EmKCs (Figure 3B). In previous work, *Timd4* and *Cd163* mRNAs were shown to be almost absent on MoKCs generated following diphteria toxin-mediated depletion of EmKCs in *Clec4f*-DTR mice, while *Vsig4* expression remained high (Scott et al., 2016). Here, we noticed *Vsig4* mRNA expression was lower in MoKCs compared to EmKCs (Figure 3B). *Clec4f* mRNA expression was also lower in MoKCs than EmKCs (Figure 3B). Notably, only a fraction of MoKCs (~40%) exhibited cell surface expression of VSIG4 (Figure 3C), and a similar observation was made for CLEC4F (Supplemental Figure 2H). In a time-course experiment, we found that the fraction of VSIG4^{+} MoKCs remained around 40% over time, while EmKCs were homogeneously VSIG4^{+} (Supplemental Figure 2I and 2J). Finally, the vast majority of MoKCs (~90%) were TIMD4^{-} as expected (Figure 3D). Thus, our findings suggest that while MoKCs generated during NASH express CLEC2 similarly to their EmKCs counterparts, they do not fully mature during diseases progression. In addition, we also noticed that MoKCs were hyperproliferative as compared to EmKCs (Figure 3E).

Next, we examined whether MoKCs would mature and be maintained for long-term after NASH regression. To address this point, NASH was induced and mice were then switched to a chow diet for 6 and 12 weeks. After 6 weeks of regression, plasma alanine aminotransferase (ALT) activity was already similar to healthy conditions (Figure 3F) and MoDMacs were no longer observed in the liver (data not shown). Concerning hepatic triglyceride content, while it was already markedly decreased after 6 weeks, 12 weeks were needed to reach the levels observed in healthy animals (Figure 3G). After 6 weeks of regression, we found that MoKCs still represented ~40-50% of the KC pool (Figure 3H), arguing that they do not represent a transient fate and can be maintained in the long-term as EmKCs. At this time, MoKCs were almost all mature VSIG4^{+} cells as observed for EmKCs (Figure 3I) but only ~15% (16.6 ± 1.2%, n=7) were TIMD4^{+}. In addition, MoKCs lost their hyperproliferative state and proliferated at rates similar to EmKCs (Figure 3J). MoKC participation to the KC pool was still effective after 12 weeks of regression (Figure 3K). They were nearly all VSIG4^{+}, with ~20% of them (20.6 ± 2%,

n=8) expressing TIMD4, and their proliferative state was also comparable to EmKCs (Figure 3L).
Overall, our findings reveal that MoKCs generated over the course of NASH development are immature but could mature and be maintained in the long-term when disease regresses. Thus, EmKCs can be replaced by MoKCs that acquire the potential to self-renew.

EmKC protection from cell death limits MoKC generation.
We next wondered whether increased EmKC death initiated MoKCs development. We indeed found a marked increase in CLEC4F$^+$ EmKC cell death during NASH as compared to healthy conditions (Figure 4A). To validate that EmKC demise led to MoKC generation, we decided to strengthen EmKC survival capacities. Therefore, we took advantage of transgenic mice overexpressing the human isoform of the death-protective factor BCL2 under control of the myeloid CD68 promoter (*Cd68-hBCL2* mice) (Gautier et al., 2009), which have increased EmKC numbers (Bouchareychas et al., 2015). To specifically modulate EmKC but not monocyte nor MoDMac death, *Cd68-hBCL2* animals were crossed to *Ccr2*$^{-/-}$ mice, irradiated at 3 Gy and transplanted with CD45.1$^+$ BM (Figure 4B). In this model, radioresistant EmKCs expressed hBCL2, while monocytes and MoDMacs did not since they were almost all derived from donor CD45.1$^+$ cells (Figure 4C). After 6 weeks of MCD diet feeding, blood Ly-6C$^+$ monocyte chimerism was ~95% in *Ccr2*$^{-/-}$ recipients and ~86% in *Cd68-hBCL2* x *Ccr2*$^{-/-}$ recipients (data not shown). At this time point, liver Ly-6C$^+$ monocyte chimerism was ~98% in *Ccr2*$^{-/-}$ recipients and ~95% in *Cd68-hBCL2* x *Ccr2*$^{-/-}$ recipients (data not shown). A 1.8-fold decrease in MoKC frequency was observed in male *Cd68-hBCL2* x *Ccr2*$^{-/-}$ recipients (Figure 4D). Absolute MoKCs numbers were also decreased, while EmKCs were increased in male *Cd68-hBCL2* x *Ccr2*$^{-/-}$ recipients (Supplemental Figure 2K). In females, MoKC frequency was decreased by 2.5-fold as compared to controls (Figure 4E), and this was also observed when absolute numbers were assessed (Supplemental Figure 2L). In conclusion, forced expression of hBCL2 in EmKCs limits their replacement by MoKCs, indicating that EmKC death facilitates the generation of MoKCs.

EmKC replacement by MoKCs limits hepatic triglyceride storage during NASH.
To further study MoKC function, we sought for transgenic tools allowing their targeting. As reported previously, *Cd207* mRNA is expressed by KCs (Lavin et al., 2014) and we validated herein its expression at the protein level (Figure 1B). To achieve inducible KC depletion, we used *Cd207*-DTR mice, known to delete skin Langerhans cells as well as lung and spleen cDC1 dendritic cells (Kissenpfennig et al., 2005). When these mice were injected with diphteria toxin (DT), EmKCs were efficiently depleted while tissue-resident macrophages in other tissues (spleen, kidney, peritoneum, lung) and blood monocytes remained unaffected (Supplemental Figure 3A). Since we also detected *Cd207* mRNA expression in MoKCs but not MoDMacs (data not shown), we thought we could generate *Ccr2*$^{-/-}$-based chimeras using *Cd207*-DTR bone marrow as donor cells to deplete MoKCs, while EmKCs and MoDMacs would remain intact. Unfortunately, DT injection was ineffective at fully depleting MoKCs in those chimeras (data not shown). Such finding is reminiscent of what was recently observed in the KC-specific *Clec4f*-cre mouse strain, in which MoKCs are not able to induce cre recombinase expression as compared to EmKCs (Scott et al., 2018). To study whether MoKCs influence NASH development in a similar way as EmKCs, we generated mice harboring either EmKCs only or a majority of MoKCs. As DT-mediated depletion of EmKCs leads to their

replacement by MoKCs (Scott et al., 2016), we used *Cd207*-DTR to generate mice bearing MoKCs following DT injection. They were compared to *Cd207*-DTR receiving boiled-inactivated DT (bDT), and thus harboring only EmKCs. As expected, MoKCs, defined as CLEC2$^+$ TIMD4$^-$ CD163$^-$ cells, represented >80% of the KC pool in chow-fed *Cd207*-DTR mice 3 weeks after DT injection (Supplemental Figure 3B). Moreover, total KC numbers were similar between bDT and DT-treated animals at this time point (Supplemental Figure 3C). While DT also depleted CD8α$^+$ and CD103$^+$ cDC1 dendritic cells in the spleen and lung of *Cd207*-DTR mice (data not shown), they were back to normal 3 weeks after DT treatment (Supplemental Figure 3D and 3E). In addition, liver cDC1 appeared normal in *Cd207*-DTR mice 3 weeks after DT treatment (Supplemental Figure 3F). Thus, at this time point, MoKCs have replaced EmKCs in DT-treated animals and the other populations affected by DT were back to normal. Next, 3 weeks after being treated with DT or bDT, *Cd207*-DTR mice were fed the MCD diet for 2 weeks (Figure 5A). We chose this time point to limit the amount of engrafted MoKCs in the control bDT-treated animals (Figure 3A) and thus maximize the difference in MoKC numbers between the 2 groups. Here, we assumed that TIMD4$^-$ KCs were all bona fide MoKCs based on our data (Figure 3D) and others previous findings (Beattie et al., 2016; Scott et al., 2018). Hence, we defined EmKCs as CLEC2$^+$ TIMD4$^+$ and MoKCs as CLEC2$^+$ TIMD4$^-$. Two weeks after MCD diet feeding, ~25% and more than 80% of KCs were TIMD4$^-$ MoKCs in bDT and DT treated animals, respectively (Figure 5B). In bDT treated controls, CLEC2$^+$ TIMD4$^-$ MoKCs were CD163$^-$ and partly VSIG4$^+$, while EmKCs were mostly CD163$^+$ and all VSIG4$^+$ (Figure 5C). In DT-treated animals, MoKCs were essentially CD163$^-$ and a significant proportion were VSIG4$^+$ (Figure 5C). Overall, lack of TIMD4 and CD163 expression ascertained the monocytic origin of KCs. After 2 weeks of MCD diet, TIMD4$^-$ CD163$^-$ MoKCs represented ~20% and ~80% in bDT and DT treated animals, respectively (Figure 5D). When a tSNE analysis was conducted in order to perform a dimensional reduction of KC diversity in DT-treated animals, two TIMD4$^+$ EmKCs subsets (cluster 3 : VSIG4$^+$ TIMD4$^+$ CD163$^-$, cluster 5 : VSIG4$^+$ TIMD4$^+$ CD163$^+$) and three TIMD4$^-$ MoKCs subsets (cluster 1 : VSIG4$^+$ TIMD4$^-$ CD163$^-$, cluster 2 : VSIG4$^+$ TIMD4$^-$ CD163$^+$, cluster 4 : VSIG4$^-$ TIMD4$^-$ CD163$^-$) were identified (Figure 5E), most likely underlying several stages of maturation in MoKCs. Next, we determined whether hepatic triglyceride content was altered when the liver was populated by a majority of MoKCs. All subsets included, we noticed a small decrease in the total KC pool in DT-treated *Cd207*-DTR mice, suggesting that the ability of MoKCs to self-maintain during NASH was slightly limited as compared to EmKCs (Figure 5F). Yet, Ly-6C$^+$ monocytes (Figure 5G), MoDMacs (Figure 5H) and neutrophils (Figure 5I) counts were unaltered. Next, we determined whether the liver pathology was altered. We observed a decrease in hepatic triglyceride storage in DT-treated *Cd207*-DTR mice (Figure 5J) while plasma ALT activity increased in these mice (Figure 5K). Thus, altered ability to store triglycerides and hepatic damage were observed when MoKCs dominate in the liver. Next, mRNA expression of key genes involved in lipid metabolism were assessed in the liver. We observed that genes involved in fatty acid synthesis (*Acaca* and *Fasn*) were unchanged (Figure 5L). By contrast, *Scd1*, which encodes for an enzyme catalyzing the conversion of toxic saturated fatty acids (SFAs) into monounsaturated fatty acids (MUFAs) that can eventually be stored as triglycerides, was decreased in DT-treated *Cd207*-DTR animals (Figure 5M). Of note, *Scd1*$^{-/-}$ animals fed a MCD diet exhibit limited hepatic triglyceride storage and increased liver damage (Li et al., 2009), as observed in our model. Genes involved in triglyceride synthesis (*Dgat1*, *Dgat2*), lipid oxidation (*Cpt1a*, *Ppara*) and fatty acid uptake (*Slc27a2*, *Slc27a4*) were similarly expressed in DT-treated *Cd207*-DTR mice

and controls (Figure 5N, 5O and 5P). Finally, we analyzed the mRNA expression of genes involved in extracellular matrix deposition, even though the timeframe of our experimental set up was too short to observe hepatic fibrosis. Indeed, the MCD diet can induce liver fibrosis when administered to mice for months (Machado et al., 2015). We observed that several pro-fibrotic mediators were elevated in the liver of DT-treated *Cd207*-DTR mice as compared to controls (Figure 5Q). Overall, mice harboring a majority of MoKCs had decreased hepatic triglyceride content, increased liver damage and a pre-fibrotic gene signature after challenged with the MCD diet for 2 weeks.

To gain further insight into the potential functional differences between EmKCs and MoKCs, we sorted these two populations from livers of wild-type mice with NASH and performed RNAseq analysis. EmKCs were also sorted from chow-fed animals. EmKCs and MoKCs were discriminated based on TIMD4 expression, as mentioned above. Comparative transcriptomic analysis revealed 4 clusters (Figure 6A). Cluster 1 discriminated EmKCs from MoKCs, and included the classical EmKC markers *Cd163*, *Cxcl13* and *Vsig4*. Cluster 2 comprised EmKC-specific genes that were slightly downregulated under NASH conditions. Overall, these 2 clusters were enriched with genes involved in the complement and coagulation cascades. EmKCs homeostasis was definitely altered upon MCD diet feeding as we noticed the induction of inflammatory genes as well as genes involved in ER stress (Supplemental Figure 4A-C), which might explain why EmKCs die during NASH (Figure 4A). Such signature was not observed in EmKCs from HFD-fed animals (Supplemental Figure 4A-C). Next, genes mutually induced in EmKCs and MoKCs during NASH composed cluster 3, and were enriched for pathways such as cytokine-cytokine receptor interaction and the lipid pathway "PPAR signaling". Of note, few differences between EmKCs and MoKCs were noted regarding the expression of genes involved in lipid metabolism (Supplemental Figure 4D-F), except a decrease in *Scd1* mRNA expression in MoKCs (Supplemental Figure 4F). This observation was consistent with the decreased cellular lipid staining observed in MoKCs, as SCD-1 favors lipid storage (Supplemental Figure 4G). Of note, MoKCs lipid loading might thus be an intermediate between MoDMacs and EmKCs. Finally, cluster 4 comprised genes strongly enriched in MoKCs, and most of these genes were involved in inflammatory processes. Indeed, pathways as cytokine-cytokine receptor interaction, chemokine signaling, NF-kappa B signaling or TNF signaling were enriched in this last cluster. Such inflammatory status of MoKCs might have favored the onset of the pre-fibrotic signature we observed in the liver of mice harboring a majority of MoKCs (Figure 5Q). In addition, we noticed that several genes encoding for known pro-fibrotic mediators (*Vegfa*, *Spp1*, *Inhba*, *Osm*, *Lgals3*, *Il10* and *Fn1*) were up-regulated in MoKCs as compared to EmKCs (Supplemental Figure 4H). Overall, a principal component analysis revealed that EmKCs from the NASH condition clearly clustered aside from naïve EmKCs, while MoKCs were definitely set apart (Figure 6B). Then, we observed that many genes known as EmKC markers, such as *Clec4f* and *Timd4*, were downregulated in EmKCs during NASH, and weakly expressed by MoKCs (Figure 6C). Along these lines, expression of genes associated with iron metabolism suggested that MoKCs were less actively engaged in erythrophagocytosis, a key EmKCs function (Supplemental Figure 4I). By contrast, *Cx3cr1* and *Ccr2* were solely found in MoKCs, indicating their monocytic origin (Figure 6C). A contamination of MoKCs by liver capsular macrophages (LCMs) that also express *Cx3cr1* (Sierro et al., 2017) was excluded since *Clec1b* (encoding CLEC2) mRNA expression was low in LCMs as observed for *Clec4f*, *Visg4*, *Cd163* and *Timd4* (Supplemental Figure 5A). Furthermore, KC subsets expression of the GFP protein in *Cx3cr1*$^{Gfp/+}$ mice fed the MCD for 6 weeks revealed that CX3CR1 promoter

activity was absent in EmKCs and only observed in the most immature VSIG4-negative MoKCs (Supplemental Figure 5B). Inflammatory genes (*Tnf*, *Cxcl1*, *Cxcl2*, *Ccl2*) were induced in EmKCs during NASH, and were even more strongly expressed in MoKCs. Additionally, genes associated with the metabolic activation of macrophages such as *Cd9*, *Trem2* and *Gpnmb* (Jaitin et al., 2019) were markedly induced in MoKCs (Figure 6C). Overall, when compared to EmKCs retrieved from the NASH condition, MoKCs were enriched with genes related to inflammatory pathways (Figure 6D). Next, we intended to further document differences between EmKCs and MoKCs using our RNAseq data. In particular, we wondered how the inflammatory hepatic environment, partly driven by lipids such as saturated fatty acids (SFAs), would impact on KC subsets. SFAs are known inducers of inflammation that engage the NLRP3 inflammasome, and we found several components of this complex were upregulated in MoKCs as compared to EmKCs (Supplemental Figure 6A). Then, we generated gene signatures characterizing the macrophage response to SFA alone or in combination with LPS, and we found they were significantly enriched in MoKCs versus EmKCs (Supplemental Figure 6B-C). This suggests MoKCs were probably more prone to lipids-induced stress and inflammation during NASH. In summary, MoKCs have a distinct transcriptional landscape characterized by an increased inflammatory status and they altered the liver response to lipids during NASH as compared to EmKCs.

Impaired EmKC survival and accelerated MoKC generation limit hepatic triglyceride content during NASH.

We next addressed how EmKCs would impact on hepatic triglyceride storage during NASH progression. To this aim, *Cd207*-DTR were fed the MCD diet for 4 weeks and then injected with bDT or DT. One day after DT injection, we found that EmKCs as well as "mature" VSIG4^{+} MoKCs were depleted, while VSIG4^{-} MoKCs were unaffected (Figure 7A). Depletion of these subsets led to decreased hepatic triglyceride storage as measured one week after bDT or DT injection (Figure 7B). Thus, KCs as a whole facilitate hepatic triglyceride storage although MoKCs were less efficient to do so than EmKCs. We next set out to identify regulators of EmKC survival whose deletion would accelerate their replacement by MoKCs. Our RNAseq analysis revealed that the anti-apoptotic gene *Bcl2l1* was expressed by EmKCs and its expression markedly increased during NASH (Figure 7C). Thus, to determine whether *Bcl2l1* expression by EmKCs would be a brake to MoKCs generation, we deleted *Bcl2l1* in EmKCs by crossing *Bcl2l1* floxed animals to *Cd207*-cre mice (Zahner et al., 2011). In the steady state, mice lacking *Bcl2l1* in KCs showed a decrease in EmKCs and harbored few MoKCs (Supplemental Figure 7A and 7B). These mice and their controls were then fed with the MCD diet for 2 weeks. After challenge, mice lacking *Bcl2l1* in EmKCs displayed an increase in the MoKC fraction among KCs (Figure 7D). Eventually, EmKC numbers were decreased (Figure 7E), while MoKCs numbers increased (Figure 7F) in *Cd207*-cre x *Bc2l1*$^{flox/flox}$ mice as compared to controls. These changes were associated with decreased triglyceride storage in the livers of *Cd207*-cre x *Bc2l1*$^{flox/flox}$ animals (Figure 7G), concomitant to lower hepatic *Scd1* mRNA expression (Figure 7H). Finally, plasma ALT activity was markedly elevated in *CD207*-cre x *Bc2l1*$^{flox/flox}$ animals as compared to controls (Figure 7I). Thus, limiting EmKC survival and favoring the generation of MoKCs ultimately impacts on hepatic lipid content and liver damage during NASH.

DISCUSSION

Under homeostatic conditions, KCs are known to self-renew locally to maintain themselves in the long-term, independently from circulating monocytes. Whether this paradigm holds true during pathological settings remains unclear. While it has been shown that KCs from monocytic origin are generated upon *Listeria monocytogenes* infection (Blériot et al., 2015), acetaminophen-induced liver injury does not drive MoKC development (Zigmond et al., 2014). Thus, MoKC generation during acute inflammatory episodes is not a consistently observed event. In addition, the impact of chronic liver diseases on KC self-maintenance remains ill-defined. Here, we asked whether metabolic liver alterations such as hepatic steatosis and its progression to NASH, the leading cause of chronic hepatopathy worldwide, would affect KC homeostasis. We now report that steatohepatitis alters the ability of KCs to self-maintain, leading to the generation of MoKCs seeding the liver in the long-term, even after disease has regressed. Thus, chronic steatohepatitis leads to permanent changes in the KC pool, with potential long-lasting impact on liver homeostasis and function.

Studying KC homeostasis first required to unequivocally discriminate them from MoDMacs accumulating during steatohepatitis. Initially, we used markers such as VSIG4, TIMD4 and CD163 previously known for their selective expression on KCs, but not MoDMacs. However, we found that CLEC2 was the most useful marker to selectively identify KCs. In fact, CLEC2 cell surface expression was similar on EmKCs and MoKCs. Of note, there is still more to learn about CLEC2 regulation as it is not well documented, although it doesn't seem to be regulated on EmKCs during liver injury (Zigmond et al., 2014). By contrast, TIMD4 and CD163 were poorly expressed by MoKCs, while VSIG4 and CLEC4F were only present on a fraction of these cells. Also, *Clec1b* (encoding CLEC2) mRNA induction by MoKCs preceded *Vsig4*, *Clec4F*, *Cd163* and *Timd4* expression in a model of experimental KC depletion (Bonnardel et al., 2019), implying CLEC2 is one of the earliest marker signing the acquisition of a KC identity. CLEC2 also permitted us to discriminate MoKCs from MoDMac. Several KC markers were induced in MoKCs, but not in MoDMacs, arguing that MoKCs mostly differ from MoDMac by their ability to integrate cues from the niche and transition toward a KC fate. Further work will be needed to develop the tools to image CLEC2^{+} cells and document MoKCs and EmKCs respective location along the hepatic sinusoids. Thus, CLEC2 was instrumental to unequivocally identify KCs independently from their origin. A recent study identified two KC subsets in the human liver based on TIMD4 expression, suggesting KC diversity might also be observed in human liver diseases (Ramachandran et al., 2019).

Here, we revealed steatohepatitis profoundly affected KC homeostasis, and their potential to self-renew was insufficient to maintain the KC pool under those chronic inflammatory conditions. Monocyte differentiation into KCs was thus necessary to maintain KC numbers similar to those observed under homeostatic conditions. We observed more EmKCs death during NASH that favored the appearance of MoKCs. Multiple aspects of NASH pathogenesis, such as lipid-induced endoplasmic reticulum stress and oxidative stress, may concur to cause KC death, as they lead to hepatocytes apoptosis (Kanda et al., 2018). We indeed observed a gene signature consistent with increased ER stress in EmKCs during NASH, which may underly their increased susceptibility to die.

MoKCs were generated in the course of steatohepatitis and we observed that they still contributed to the KC pool after disease had regressed. While a majority of MoKCs found during NASH were not fully mature, MoKCs were maintained and matured after NASH regression. Their participation to the KC pool remained stable even 3 months after

disease regression. MoKCs thus acquired the full spectrum of KC characteristics and in particular the ability to self-renew, although we did not rule out that continuous MoKCs generation occurred during NASH regression. These findings are conflicting with a recent report claiming that the changes observed within the liver macrophage pool during MCD diet-induced NASH were transient (Devisscher et al., 2017). In this study, macrophages were defined as F4/80^{+} Ly-6C^{lo} cells, and the macrophage pool was further subdivided into 3 populations, namely, CLEC4F^{+} TIMD4^{+}, CLEC4F^{+} TIMD4^{-} and CLEC4F^{-} TIMD4^{-} cells. During disease regression, the two latter populations were lost and only a few TIMD4^{-} macrophages were left after regression. Monocyte tracking was not performed in this study, which might explain the discrepancy. In our study, following monocyte fate turned out to be crucial because the cell surface phenotype of MoKCs changed as they matured during regression. Overall, MoKCs were capable to seed the liver and be maintained in the long-term. These findings revealed that the ability of monocytes to fill the niche after KC death, as happens after experimental KC depletion (Scott et al., 2016), can similarly be observed in certain physiopathological contexts such as NASH.

In order to compare KC subsets impact on NASH development, we generated mice harboring mostly MoKCs or only EmKCs. We noticed from our RNAseq analysis that MoKCs were enriched for genes involved in cellular stress and activation, which would need to be further substantiated at the protein level. Then, we observed that MoKCs limited hepatic triglyceride storage upon MCD diet feeding while increasing liver damage as assessed by plasma transaminase activity. Such decreased steatosis most likely reflected limited storage into hepatocytes rather than KCs given that hepatocytes occupy a much larger volume and store TGs as macrovesicular lipid droplets as compared to microvesicular droplets in KCs. Finally, we found that liver expression of *Scd1*, encoding for an enzyme that limits the accumulation of toxic lipids and favors triglyceride storage, was decreased when MoKCs dominated. Further work would be needed to address its specific regulation in hepatocytes. Of note, the phenotype of *Scd1*$^{-/-}$ animals fed the MCD diet mirrored our observations, with limited liver triglyceride storage and increased hepatic damage (Li et al., 2009). *Scd1*$^{-/-}$ animals had increased SFA to MUFA ratio and were impaired in their ability to partition excess lipid into MUFAs that can be safely stored (Li et al., 2009). Of note, the slight decrease in MoKCs numbers observed after MCD feeding could also have participated to reduce triglyceride accumulation in our model. In addition, we observed a decrease in hepatic triglyceride storage when we specifically depleted EmKCs and VSIG4^{+} MoKCs in established NASH. Finally, we revealed that limiting EmKC survival and favoring their replacement by MoKCs dampened hepatic TG content and increased liver damage. We can thus assign an accessory function to EmKCs as facilitators of hepatic lipid storage as triglycerides, an adaptation to lipid overload that limits lipid toxicity and confers tissue protection. Nonetheless, our results revealed that MoKCs might not be as effective as EmKCs to promote this lipid storage. This finding highlights a differential functional impact of KCs on liver disease depending on their origin.

Overall, our work revealed steatohepatitis had a major and long-lasting impact on the ability of EmKCs to self-maintain that in turn impacted on the liver response to lipid overload.

ACKNOWLEDGMENTS
This work was supported by grants to ELG from the Agence Nationale pour la Recherche (ANR-15-CE14-0015-02, ANR-17-CE14-0009-02, ANR-17-CE14-0023-01) and from the city of Paris (Emergence(s) program). Sophie Tran and Melissa Ouhachi both received a one-year doctoral fellowship from the Nouvelle Société Française d'Athérosclérose (NSFA).

AUTHOR CONTRIBUTIONS
S.T., I.B., S.D., M.M., A.G., M.O. designed and performed experiments, analyzed data. L.P., designed and performed experiments, analyzed data, provided intellectual input. G.M., provided mice and intellectual input, edited the manuscript. P.L., provided mice. A.B., provided mice and technical expertise. W.L.G., provided mice. L.Y.C and F.S. provided intellectual input and edited the manuscript. B.E.C, provided mice and edited the manuscript. T.H., provided intellectual input, provided mice, designed experiments, interpreted data and edited the manuscript. E.L.G., conceptualized and supervised the study, designed and performed experiments, analyzed and interpreted data, and wrote the manuscript.

DECLARATION OF INTERESTS
The authors declare no competing interests.

FIGURE LEGENDS
Figure 1. Discriminating Kupffer cells from inflammatory monocyte-derived macrophages in a mouse model of NASH. ***A***. Flow cytometry analysis of CD64^{+} CD11b^{lo} KCs also all positive for F4/80. ***B***. Expression of cell surface markers VSIG4, CLEC2, CD207, TIMD4 and CD163 on CD64^{+} F4/80^{hi} KCs. ***C***. Liver CLEC2^{hi} cells are all *bona-fide* CD11b^{lo} F4/80^{hi} KCs. ***D-E***. Plasma ALT (D) and liver triglyceride content (E) in mice fed a chow or the MCD diet for 6 weeks (n=4 per group). ***F***. Flow cytometry analysis of KCs (CLEC2^{hi} CD11b^{lo}), monocyte-derived inflammatory macrophages (CLEC2^{lo} CD11b^{hi} CD11c^{+} CD64^{+}), Ly-6C^{+} monocytes (CLEC2^{lo} CD11b^{hi} CD64^{-} Ly-6C^{hi} CD11b^{int}) and neutrophils (CLEC2^{lo} CD11b^{hi} CD64^{-} Ly-6C^{int} CD11b^{hi}) in chow and MCD-fed animals. ***G-H***. Intracellular lipids stained by Bodipy (G) and percentage of Ki-67^{+} (H) KCs in mice fed a chow or the MCD diet for 6 weeks (n=4-6 per group). ***I***. KCs, monocyte-derived inflammatory macrophages (MoDMacs) and Ly-6C^{+} monocytes quantification in mice fed a chow or the MCD diet for 6 weeks (n=4 per group). ***J***. Flow cytometry plots illustrating the loss of MoDMacs in *Ccr2*$^{-/-}$ animals fed the MCD diet for 6 weeks as compared to controls. ***K***. KCs, MoDMacs and Ly-6C^{+} monocytes quantification in WT and *Ccr2*$^{-/-}$ mice fed a chow or the MCD diet for 6 weeks (n=7-8 per group).
See also Figure S1.

Figure 2. Monocyte-derived KCs participate to the KC pool during NASH. ***A***. Generation of low-irradiation chimeras using *Ccr2*$^{-/-}$ mice as recipients and bone marrow cells from CD45.1 mice. ***B***. Flow cytometry analysis of blood monocytes chimerism. ***C-D***. Chimerism in blood total leukocytes, T cells, B cells, neutrophils (PMNs), Ly-6C^{+} monocytes (Mo Ly-6C^{+}) and Ly-6C^{-} monocytes (Mo Ly-6C^{-}) 2 weeks (C) or 6 weeks (D) after transplantation (BMT) (n=6-8). ***E-F***. Flow cytometry analysis (E) and quantification (F) of KCs and MoDMacs chimerism in *Ccr2*$^{-/-}$-based chimeras fed a chow or the MCD diet for 6 weeks (n=8-10). ***G***. Correlation between monocytes-derived KCs (KCs CD45.1^{+}) and MoDMacs frequencies in MCD-fed animals (n=8). ***H***. Chimerism in

lung alveolar macrophages of chow (n=7) and MCD-fed *Ccr2*$^{-/-}$-based chimeras (n=6). ***I***. Parabiosis-mediated pairing of WT CD45.1 or WT *eCFP* transgenic with *Ccr2*$^{-/-}$ CD45.2 animals. ***J***. Chimerism (CD45.1^{+} or eCFP^{+} cells) in Ly-6C^{+} monocytes (Mo Ly-6C^{+}), KCs, MoDMacs and lung alveolar macrophages of the *Ccr2*$^{-/-}$ parabionts in chow (n=3) and MCD-fed animals (n=5). ***K-L***. Strategy (K) and KCs chimerism (L) in *Ccr2*$^{-/-}$-based chimeras fed a chow (n=7) or a HFD (n=10) for 14 weeks. ***M-N***. Strategy (M) and KCs chimerism (N) in *Ccr2*$^{-/-}$-based chimeras fed a chow (n=3) or a CDA-HFD (n=4) for 4 weeks.
See also Figure S2.

Figure 3. Monocyte-derived KCs mature and maintain in the long-term after NASH regression. ***A***. MoKCs frequency in CLEC2^{+} KCs in *Ccr2*$^{-/-}$-based chimeras fed the MCD diet for 2 to 6 weeks (n=3-6 per time point). ***B***. qPCR analysis of KC markers (*Clec4f*, *Cd163* and *Vsig4*) in EmKCs (CD11b^{lo} CLEC2^{hi} CD45.1^{-}) sorted from chow-fed animals (chow KC) (n=4) as well as EmKCs (n=5) and MoKCs (CD11b^{lo} CLEC2^{hi} CD45.1^{+}, n=6) sorted from mice fed the MCD diet for 6 weeks. MoDMacs from MCD-fed animals were also sorted and analyzed (n=5). ***C***. Cell surface expression of VSIG4 on EmKCs, MoKCs and MoDMacs in *Ccr2*$^{-/-}$-based chimeras fed the MCD diet for 6 weeks (n=7). ***D***. Cell surface expression of TIMD4 on EmKCs and MoKCs in *Ccr2*$^{-/-}$-based chimeras fed the MCD diet for 6 weeks. ***E***. EmKC and MoKC proliferative status in *Ccr2*$^{-/-}$-based chimeras fed the MCD diet for 6 weeks (n=6). ***F-G***. Plasma ALT activity (F) and hepatic triglyceride content (G) in *Ccr2*$^{-/-}$-based chimeras fed chow (n=4-8) or MCD diet (n=9-16) for 6 weeks and *Ccr2*$^{-/-}$-based chimeras fed MCD diet for 6 weeks and then chow diet for another 6 (ALT and TG, n=10-12) or 12 weeks (TG, n=7) to induce NASH regression. ***H***. Frequency of MoKCs in the KC pool in *Ccr2*$^{-/-}$-based chimeras fed MCD diet for 6 weeks (Baseline, n=12) and *Ccr2*$^{-/-}$-based chimeras fed MCD diet for 6 weeks and then chow diet for another 6 weeks (regression, n=8). ***I-J***. Frequency of EmKCs and MoKCs expressing VSIG4 (I) or Ki-67 (J) in *Ccr2*$^{-/-}$-based chimeras fed MCD diet for 6 weeks (Baseline, n=13) and *Ccr2*$^{-/-}$-based chimeras fed MCD diet for 6 weeks and then chow diet for another 6 weeks (regression, n=9-10). ***K***. Frequency of MoKCs in the KC pool in *Ccr2*$^{-/-}$-based chimeras fed MCD diet for 6 weeks (Baseline, n=5) and *Ccr2*$^{-/-}$-based chimeras fed MCD diet for 6 weeks and then a chow diet for another 12 weeks (regression, n=6). ***L***. EmKC and MoKC proliferation status in *Ccr2*$^{-/-}$-based chimeras fed MCD diet for 6 weeks and then chow diet for another 12 weeks (n=6).
See also Figure S2.

Figure 4. EmKC protection from cell death limits MoKC generation. ***A***. Detection and quantification of dying TUNEL^{+} CLEC4F^{+} EmKCs on frozen liver sections of chow and MCD-fed animals (n=6 per condition). ***B***. Chimeras used to protect EmKCs from death. ***C***. Table recapitulating the origin and genotype of EmKCs, MoKCs and MoDMacs in chimeras. ***D-E***. Frequency of MoKCs in male (D) (n=17-18 per group) and female (E) (n=10-13 per group) *Ccr2*$^{-/-}$- and *Cd68-hBCL2* x *Ccr2*$^{-/-}$-based chimeras after 6 weeks of MCD diet.
See also Figure S2.

Figure 5. EmKC replacement by MoKCs limited hepatic triglyceride storage during NASH. ***A***. Strategy used to generate mice bearing mostly EmKCs or MoKCs. ***B***. Flow cytometry analysis and quantification of TIMD4^{-} KCs (MoKC) frequency among KCs after 2 weeks of MCD diet in *Cd207*-DTR animals previously injected with bDT (n=7) or DT

(n=9). ***C***. Flow cytometry analysis of TIMD4, CD163 and VSIG4 expression on EmKCs and MoKCs after 2 weeks of MCD diet in *Cd207*-DTR animals previously injected with bDT or DT. ***D***. Flow cytometry analysis and quantification of TIMD4^{-} CD163^{-} MoKCs frequency after 2 weeks of MCD diet in *Cd207*-DTR animals previously injected with bDT (n=7) or DT (n=9). ***E*** t-SNE analysis of KC diversity based on TIMD4, CD163 and VSIG4 expressions after 2 weeks of MCD diet in *Cd207*-DTR animals that were previously injected with active DT. FACS histograms highlight the expression of TIMD4, CD163 and VSIG4 in the different clusters identified. ***F-K***. Liver KC (F), Ly-6C^{+} monocyte (G), MoDMac (H) and neutrophils (PMNs) (I) numbers as well as hepatic triglyceride content (J) and plasma ALT activity (K) after 2 weeks of MCD diet in *Cd207*-DTR animals previously injected with bDT (n=9-13) or DT (n=13-20). ***L-Q***. Hepatic mRNA expression of *Acaca* and *Fasn* (L), *Scd1* (M), *Dgat1* and *Dgat2* (N), *Cpt1a* and *Ppara* (O), *Slc27a2* and *Slc27a4* (P) as well as *Col1a1, Col3a1, Ctgf, Lox* and *Loxl2* (Q) were measured after 2 weeks of MCD diet in *Cd207*-DTR animals previously injected with bDT (n=6-7) or DT (n=6-8).
See also Figure S3.

Figure 6. Transcriptional profiling of KC subsets. ***A***. K-means clustering analysis of KC subsets found in control and NASH conditions revealed 4 clusters. Representative genes as well as pathways enriched in those clusters were depicted. ***B***. Principal component analysis (PCA) of EmKCs retrieved from chow-fed animals (n=6) as well as EmKCs (n=6) and MoKCs (n=7) isolated from mice fed MCD diet for 6 weeks. ***C***. Heat map of keys genes discriminating EmKCs from MoKCs. ***D***. Pathways enriched in MoKCs compared to EmKCs during NASH.
See also Figures S4, S5 and S6.

Figure 7. Modulation of KC subsets and its impact on NASH. ***A***. Strategy used to deplete KCs in mice with established NASH and flow cytometry analysis of EmKCs (TIMD4^{+} VSIG4^{+}), "mature" MoKCs (TIMD4^{-} VSIG4^{+}) and "immature" MoKCs (TIMD4^{-} VSIG4^{-}) 24 hours after *Cd207*-DTR animals with established steatohepatitis were injected with bDT (n=3) or DT (n=3). The bar graph shows KC subsets quantification. ***B***. Hepatic triglycerides content one week after *Cd207*-DTR animals with established steatohepatitis were injected with bDT (n=8) or DT (n=8). ***C***. RNAseq data of *Bcl2l1* mRNA expression in EmKCs under chow (n=6) and MCD-fed conditions (n=6). ***D***. Flow cytometry analysis and quantification of MoKCs in animals lacking the anti-apoptotic gene *Bcl2l1* in EmKCs (*CD207*-cre x *Bc2l1*$^{flox/flox}$ mice, n=10) fed the MCD diet for 2 weeks as compared to controls (*Bc2l1*$^{flox/flox}$ mice, n=6). ***E-F***. Absolute quantification of EmKCs (E) and MoKCs (F) in *CD207*-cre x *Bc2l1*$^{flox/flox}$ mice (n=10) and *Bc2l1*$^{flox/flox}$ controls (n=6) fed the MCD diet for 2 weeks. ***G***. Hepatic triglycerides content in *CD207*-cre x *Bc2l1*$^{flox/flox}$ mice (n=9) and *Bc2l1*$^{flox/flox}$ control (n=6) fed the MCD diet for 2 weeks. ***H***. *Scd1* mRNA expression in the liver of *CD207*-cre x *Bc2l1*$^{flox/flox}$ mice (n=8) and *Bc2l1*$^{flox/flox}$ controls (n=8) fed the MCD diet for 2 weeks. ***I***. Plasma ALT activity in *CD207*-cre x *Bc2l1*$^{flox/flox}$ mice (n=7) and *Bc2l1*$^{flox/flox}$ controls (n=8) fed the MCD diet for 2 weeks.
See also Figure S7.

STAR METHODS

RESOURCE AVAILABILITY

Lead Contact

Further information and requests for resources and reagents should be directed to and will be fulfilled by the Lead Contact, Emmanuel Gautier (emmanuel-laurent.gautier@inserm.fr).

Materials Availability

This study did not generate new unique reagents.

Data and Code Availability

The accession number for the RNAseq data generated in this study was deposited under the accession number GSE138778.

EXPERIMENTAL MODEL AND SUBJECT DETAILS

Mouse strains used in the study.

Wild-type C57BL/6J mice were from Janvier Labs. CD45.1 (Ly5.1, B6.SJL-*Ptprc*^{a}*Pepc*^{b}/BoyCrl) and *Ob/Ob* (B6.Cg-*Lep*^{ob}/J) mice were from Charles River. *Ccr2*$^{-/-}$ (B6.129S4-*Ccr2*^{tm1Ifc}/J), homozygous *eCFP* transgenic (B6.129(ICR)-Tg(CAG-ECFP)CK6Nagy/J), hemizygous *Cx3cr1*$^{Gfp/+}$ (B6.129P2(Cg)-*Cx3cr1*^{tm1Litt}/J) and homozygous *Cd207*-DTR (B6.129S2-*Cd207*$^{tm3(DTR/GFP)Mal}$/J) mice were from the Jackson Laboratory. *Cd68*-hBCL2 mice previously generated by our team (Gautier et al., 2009) were bred in-house to *Ccr2*$^{-/-}$ animals. Floxed *Bcl2l1* animals (provided by Edmund B. Rucker) were bred to *Cd207*-cre mice (Zahner et al., 2011) to obtain *Cd207*-cre x *Bcl2l1*$^{flox/flox}$ animals.

Animal housing and diets used.

Mice were maintained on a 12-hour light and dark cycle with ad libitum access to water and standard chow diet (no. 5058; Lab-Diet). For steatohepatitis studies, animals were fed a methionine and choline-deficient diet (MCD, A02082002BR, Research Diets) or a choline-deficient high fat diet (CDA-HFD, A06071302, Research Diets). Alternatively, steatosis was induced by high fat diet feeding (HFD, D12492, Research Diets). Diet duration was indicated in the text and/or figure legends.

All animal procedures were in accordance with the Guide for the Care and Use of Laboratory Animals published by the European Commission Directive 86/609/EEC and given authorization from the French Ministry of Research.

METHOD DETAILS

Total body irradiation and bone marrow transplantation.

Ccr2$^{-/-}$ mice were exposed to 3Gy total body irradiation. Bone marrow cells were harvested from donor mice by gently flushing their femurs and 5 to 10 x 10^6 cells were intravenously injected into each recipient mice. A two weeks-recovery period was observed to ensure donor bone marrow engraftment and blood monocytes reconstitution.

Parabiosis

Parabiotic mice were generated using 6 to 8 weeks old weight-matched CD45.2$^+$ (C57BL/6J or *Ccr2*$^{-/-}$) and CD45.1$^+$ (C57BL/6) female mice. One month after surgery mice were fed the MCD diet for 6 weeks.

Diphteria toxin (DT) injection in *Cd207*-DTR mice.
Kupffer cells were depleted following intraperitoneal DT injection (1µg per mouse) in homozygous *Cd207*-DTR mice. When long-term experiments were conducted, two DT injections were performed one day apart in order to maximize EmKCs depletion and their replacement by MoKCs. *Cd207*-DTR mice injected with boiled, heat-inactivated DT (bDT) were used as controls.

Plasma alanine aminotransferase activity.
Plasma alanine aminotransferase (ALT) activity was determined using a UV test kit (ALAT GPT FS, Diasys) run on a Konelab analyzer (Thermo Fisher Scientific).

Liver lipid extraction and triglycerides determination.
Frozen liver samples (~ 50 mg) were homogenized in a chloroform/methanol mixture (3:2; 1 mL per 50 mg of tissue) using a tissue homogenizer (Precellys, Bertin Technologies) and lipids were extracted overnight. After centrifugation (20 min x 2200 rpm) at 4°C, an aliquot of the extract was combined (1:1) with 1% Triton in chloroform. After drying, a commercially available kit (Diasys) was used for colorimetric quantification of triglycerides.

Tissue processing and cell suspensions preparation.
Spleens, lungs and kidneys were harvested from PBS-perfused animals and digested in Hanks' Balanced Salt Solution (HBSS, no calcium and magnesium) containing fetal bovine serum (3%) and collagenase D (2.5 mg/ml, Sigma) as previously described (Gautier et al., 2012b). Circulating leukocytes preparation and peritoneal lavage were performed as previously described (Gautier et al., 2013). Livers were collected from mice perfused with PBS, placed in 3 mL of HBSS containing collagenase D (2.5 mg/mL, Sigma) and DNase (10 U/mL, Sigma), minced with scissors, run on the GentleMACS dissociator and incubated for 30 min at 37°C under agitation. Samples were then run on the GentleMACS dissociator for a second time. Cell suspensions were passed through a 100 µm filter before staining.

Flow cytometry.
Antibodies were purchased from BioLegend, Thermo Fisher Scientific, R&D Systems and BD Biosciences. The following markers and clones were used: CD115 (AFS98), CD11c (N418), MHC-II (M5/114.15.2), CD11b (M1/70), CD45 (30-F11), Gr-1 (RB6-8C5), Ly-6C (HK1.4), CD64 (X54-5/7.1), CD64 (FAB20741P), VSIG4 (NLA14), CD207 (4C7), CLEC4F (AF2784), CD163 (TNKUPJ), F4/80 (BM8), TIMD4 (RMT4-54), CLEC2 (17D9), Ki-67 (B56), CD45.1 (A20), CD19 (1D3), TCRβ (H57-597), CD103 (2E7), Siglec-F (E50-2440) and CD8a (53-6.7).
Cell suspensions were stained with appropriate antibodies for 30 min on ice. Draq7 was used to exclude dead cells. Intracellular Ki-67 staining was performed using the Foxp3 staining kit from Thermo Fisher Scientific. Bodipy staining was performed on cells fixed using the Cytofix/Cytoperm™ kit from BD Biosciences.
To calculate absolute cell counts, a fixed number of nonfluorescent beads (10000, 10-µm polybead carboxylate microspheres from Polysciences) was added to each tube. The

formula number of cells = (number of acquired cells × 10,000) ÷ (number of acquired beads) was used. Cell counts were finally expressed as a number of cells per milligram of tissue or per milliliter of blood.
Data were acquired on a BD LSRFortessa™ flow cytometer (BD Biosciences) and analyzed with FlowJo software (Tree Star). The dimensionality reduction algorithm tSNE (t-Distributed Stochastic Neighbor Embedding) was run using the plugin integrated in FlowJo. Cell sorting was performed on a BD FACSAria II™ cell sorter.

Liver neutral lipid staining and *in situ* analysis of Kupffer cells death.
Livers were collected, fixed in 4% paraformaldehyde solution followed by incubation in a sucrose solution (30% in PBS) at 4°C. Livers were then embedded in Tissue-Tek OCT compound and sectioned. Frozen sections (8 µm) were rinsed in PBS and incubated with Bodipy (0.1mg/ml in PBS) for 30 min to label neutral lipids. After washing in PBS, the sections were counterstained for nuclei with DAPI.
Frozen liver sections (8 µm) were rinsed in PBS and dead cells were labelled using the *In-Situ* Cell Death Detection Kit (TMR red, Sigma). Kupffer cells were labelled with an anti-CLEC4F antibody (goat polyclonal, R&D Systems) following by anti-goat Cy2 (Jackson ImmunoResearch) while nuclei were stained with DAPI.
Images were captured using a Zeiss AxioImagerM2 microscope and the AxioVision Zeiss software. Images were processed using the open-source Fiji software.

qPCR analysis of flow cytometry-sorted cells.
Total RNA preparation was performed from 20 000 sorted cells using the RNeasy Plus micro kit (QIAGEN). RNA was reverse transcribed using the SuperScript VILO cDNA synthesis kit (Thermo Fisher Scientific). Quantitative PCR analyses were performed using a LightCycler® 480 real-time PCR system and dedicated software (Roche). Initial differences in mRNA quantities were controlled using reference mouse genes *Hprt*, *Rpl13a*, and *Nono*. Gene expression was normalized to those 3 housekeeping genes using the Roche LightCycler® 480 software. Primers sequences are available upon request.

qPCR analysis of liver samples.
Total RNA preparation was performed using the NucleoSpin RNA Plus kit (MACHEREY-NAGEL). RNA was reverse transcribed using the Transcriptor First Strand cDNA Synthesis Kit (Roche). Quantitative PCR analyses were performed using a LightCycler® 480 real-time PCR system and dedicated software (Roche). Gene expression was normalized to at least 3 housekeeping genes using the Roche LightCycler® 480 software. Primers sequences are available upon request.

Published RNAseq and microarray datasets.
Expression of several genes was extracted from previous profiling of tissue resident macrophage populations (GSE37448, GSE15907, GSE63340, GSE75225, GSE55606, E-MTAB-5932, PRJNA483744) (Gautier et al., 2012a; Lavin et al., 2014; Morgantini et al., 2019). Other datasets were used (GSE77104, GSE117115) to generate specific gene signatures.

RNAseq on flow cytometry-sorted KCs.
Total RNA preparation was performed from 5 x 10^3 sorted KCs using the RNeasy Plus Micro Kit (Qiagen). cDNA libraries were generated using SMART-Seq v4 Ultra Low Input

RNA Kit for Sequencing (Takara). RNA-Seq libraries were sequenced on an Illumina NovaSeq 6000 (30 million reads per sample).
RNA-Seq analysis was completed using the Eoulsan pipeline (Jourdren et al., 2012). The STAR index was used to map raw reads to the genome and data normalization was performed with DESeq2. A LIMMA analysis was conducted to select differentially expressed genes with a 2-fold change cutoff between at least two conditions. Adjusted p value for multiple gene testing were used. Annotated genes with a count mean over 100 in at least one condition and a coefficient of variation of more than 0.5 between at least two conditions were retained. Principal component analysis, K-means clustering and GSEA analysis were performed using the Phantasus web platform. Cluster number was determined using the R cluster package. The R package ClusterProfiler and the web platform Enrichr were used for pathway analysis and illustration. Data were deposited at NCBI under the accession number GSE138778.

QUANTIFICATION AND STATISTICAL ANALYSIS

Statistical significance of differences was performed using GraphPad Prism (GraphPad Software). Two-tailed Student's t-test was used to assess the statistical significance of the difference between means of two groups. Experiments were repeated at least twice. When more than 2 groups were studied, analysis of variance was performed followed by Newman-Keuls as post-hoc test. Graphs depicted the mean ± SEM. Statistical significance is represented as follows: *P<0.05, **P<0.01, ***P<0.001 and ****P<0.0001.

REFERENCES

Beattie, L., Sawtell, A., Mann, J., Frame, T.C.M., Teal, B., de Labastida Rivera, F., Brown, N., Walwyn-Brown, K., Moore, J.W.J., MacDonald, S., et al. (2016). Bone marrow-derived and resident liver macrophages display unique transcriptomic signatures but similar biological functions. J. Hepatol. *65*, 758–768.

Blériot, C., Dupuis, T., Jouvion, G., Eberl, G., Disson, O., and Lecuit, M. (2015). Liver-resident macrophage necroptosis orchestrates type 1 microbicidal inflammation and type-2-mediated tissue repair during bacterial infection. Immunity *42*, 145–158.

Bonnardel, J., T'Jonck, W., Gaublomme, D., Browaeys, R., Scott, C.L., Martens, L., Vanneste, B., De Prijck, S., Nedospasov, S.A., Kremer, A., et al. (2019). Stellate Cells, Hepatocytes, and Endothelial Cells Imprint the Kupffer Cell Identity on Monocytes Colonizing the Liver Macrophage Niche. Immunity.

Bouchareychas, L., Pirault, J., Saint-Charles, F., Deswaerte, V., Le Roy, T., Jessup, W., Giral, P., Le Goff, W., Huby, T., Gautier, E.L., et al. (2015). Promoting macrophage survival delays progression of pre-existing atherosclerotic lesions through macrophage-derived apoE. Cardiovasc. Res. *108*, 111–123.

Devisscher, L., Scott, C.L., Lefere, S., Raevens, S., Bogaerts, E., Paridaens, A., Verhelst, X., Geerts, A., Guilliams, M., and Van Vlierberghe, H. (2017). Non-alcoholic steatohepatitis induces transient changes within the liver macrophage pool. Cell. Immunol. *322*, 74–83.

Gautier, E.L., Huby, T., Witztum, J.L., Ouzilleau, B., Miller, E.R., Saint-Charles, F., Aucouturier, P., Chapman, M.J., and Lesnik, P. (2009). Macrophage apoptosis exerts divergent effects on atherogenesis as a function of lesion stage. Circulation *119*, 1795–1804.

Gautier, E.L., Shay, T., Miller, J., Greter, M., Jakubzick, C., Ivanov, S., Helft, J., Chow, A., Elpek, K.G., Gordonov, S., et al. (2012a). Gene-expression profiles and transcriptional regulatory pathways that underlie the identity and diversity of mouse tissue macrophages. Nat. Immunol. *13*, 1118–1128.

Gautier, E.L., Chow, A., Spanbroek, R., Marcelin, G., Greter, M., Jakubzick, C., Bogunovic, M., Leboeuf, M., van Rooijen, N., Habenicht, A.J., et al. (2012b). Systemic analysis of PPARγ in mouse macrophage populations reveals marked diversity in expression with critical roles in resolution of inflammation and airway immunity. J. Immunol. Baltim. Md 1950 *189*, 2614–2624.

Gautier, E.L., Ivanov, S., Lesnik, P., and Randolph, G.J. (2013). Local apoptosis mediates clearance of macrophages from resolving inflammation in mice. Blood *122*, 2714–2722.

Gomez Perdiguero, E., Klapproth, K., Schulz, C., Busch, K., Azzoni, E., Crozet, L., Garner, H., Trouillet, C., de Bruijn, M.F., Geissmann, F., et al. (2015). Tissue-resident macrophages originate from yolk-sac-derived erythro-myeloid progenitors. Nature *518*, 547–551.

Hardy, T., Oakley, F., Anstee, Q.M., and Day, C.P. (2016). Nonalcoholic Fatty Liver Disease: Pathogenesis and Disease Spectrum. Annu. Rev. Pathol. *11*, 451–496.

Hoeffel, G., Chen, J., Lavin, Y., Low, D., Almeida, F.F., See, P., Beaudin, A.E., Lum, J., Low, I., Forsberg, E.C., et al. (2015). C-Myb(+) erythro-myeloid progenitor-derived fetal monocytes give rise to adult tissue-resident macrophages. Immunity *42*, 665–678.

Huang, W., Metlakunta, A., Dedousis, N., Zhang, P., Sipula, I., Dube, J.J., Scott, D.K., and O'Doherty, R.M. (2010). Depletion of liver Kupffer cells prevents the development of diet-induced hepatic steatosis and insulin resistance. Diabetes *59*, 347–357.

Jaitin, D.A., Adlung, L., Thaiss, C.A., Weiner, A., Li, B., Descamps, H., Lundgren, P., Bleriot, C., Liu, Z., Deczkowska, A., et al. (2019). Lipid-Associated Macrophages Control Metabolic Homeostasis in a Trem2-Dependent Manner. Cell *178*, 686-698.e14.

Jenne, C.N., and Kubes, P. (2013). Immune surveillance by the liver. Nat. Immunol. *14*, 996–1006.

Jourdren, L., Bernard, M., Dillies, M.-A., and Le Crom, S. (2012). Eoulsan: a cloud computing-based framework facilitating high throughput sequencing analyses. Bioinforma. Oxf. Engl. *28*, 1542–1543.
Kanda, T., Matsuoka, S., Yamazaki, M., Shibata, T., Nirei, K., Takahashi, H., Kaneko, T., Fujisawa, M., Higuchi, T., Nakamura, H., et al. (2018). Apoptosis and non-alcoholic fatty liver diseases. World J. Gastroenterol. *24*, 2661–2672.
Kissenpfennig, A., Henri, S., Dubois, B., Laplace-Builhé, C., Perrin, P., Romani, N., Tripp, C.H., Douillard, P., Leserman, L., Kaiserlian, D., et al. (2005). Dynamics and function of Langerhans cells in vivo: dermal dendritic cells colonize lymph node areas distinct from slower migrating Langerhans cells. Immunity *22*, 643–654.
Krenkel, O., and Tacke, F. (2017). Liver macrophages in tissue homeostasis and disease. Nat. Rev. Immunol.
Lavin, Y., Winter, D., Blecher-Gonen, R., David, E., Keren-Shaul, H., Merad, M., Jung, S., and Amit, I. (2014). Tissue-resident macrophage enhancer landscapes are shaped by the local microenvironment. Cell *159*, 1312–1326.
Li, Z.Z., Berk, M., McIntyre, T.M., and Feldstein, A.E. (2009). Hepatic lipid partitioning and liver damage in nonalcoholic fatty liver disease: role of stearoyl-CoA desaturase. J. Biol. Chem. *284*, 5637–5644.
Machado, M.V., Michelotti, G.A., Xie, G., Almeida Pereira, T., de Almeida, T.P., Boursier, J., Bohnic, B., Guy, C.D., and Diehl, A.M. (2015). Mouse models of diet-induced nonalcoholic steatohepatitis reproduce the heterogeneity of the human disease. PloS One *10*, e0127991.
Mass, E., Ballesteros, I., Farlik, M., Halbritter, F., Günther, P., Crozet, L., Jacome-Galarza, C.E., Händler, K., Klughammer, J., Kobayashi, Y., et al. (2016). Specification of tissue-resident macrophages during organogenesis. Science *353*.
Morgantini, C., Jager, J., Li, X., Levi, L., Azzimato, V., Sulen, A., Barreby, E., Xu, C., Tencerova, M., Näslund, E., et al. (2019). Liver macrophages regulate systemic metabolism through non-inflammatory factors. Nat. Metab. *1*, 445–459.
Ramachandran, P., Dobie, R., Wilson-Kanamori, J.R., Dora, E.F., Henderson, B.E.P., Luu, N.T., Portman, J.R., Matchett, K.P., Brice, M., Marwick, J.A., et al. (2019). Resolving the fibrotic niche of human liver cirrhosis at single-cell level. Nature *575*, 512–518.
Reid, D.T., Reyes, J.L., McDonald, B.A., Vo, T., Reimer, R.A., and Eksteen, B. (2016). Kupffer Cells Undergo Fundamental Changes during the Development of Experimental NASH and Are Critical in Initiating Liver Damage and Inflammation. PloS One *11*, e0159524.
Scott, C.L., Zheng, F., De Baetselier, P., Martens, L., Saeys, Y., De Prijck, S., Lippens, S., Abels, C., Schoonooghe, S., Raes, G., et al. (2016). Bone marrow-derived monocytes give rise to self-renewing and fully differentiated Kupffer cells. Nat. Commun. *7*, 10321.
Scott, C.L., T'Jonck, W., Martens, L., Todorov, H., Sichien, D., Soen, B., Bonnardel, J., De Prijck, S., Vandamme, N., Cannoodt, R., et al. (2018). The Transcription Factor ZEB2 Is Required to Maintain the Tissue-Specific Identities of Macrophages. Immunity *49*, 312-325.e5.
Sierro, F., Evrard, M., Rizzetto, S., Melino, M., Mitchell, A.J., Florido, M., Beattie, L., Walters, S.B., Tay, S.S., Lu, B., et al. (2017). A Liver Capsular Network of Monocyte-Derived Macrophages Restricts Hepatic Dissemination of Intraperitoneal Bacteria by Neutrophil Recruitment. Immunity *47*, 374-388.e6.
Surewaard, B.G.J., Deniset, J.F., Zemp, F.J., Amrein, M., Otto, M., Conly, J., Omri, A., Yates, R.M., and Kubes, P. (2016). Identification and treatment of the Staphylococcus aureus reservoir in vivo. J. Exp. Med. *213*, 1141–1151.
Theurl, I., Hilgendorf, I., Nairz, M., Tymoszuk, P., Haschka, D., Asshoff, M., He, S.,

Gerhardt, L.M.S., Holderried, T.A.W., Seifert, M., et al. (2016). On-demand erythrocyte disposal and iron recycling requires transient macrophages in the liver. Nat. Med. *22*, 945–951.
Wolf, M.J., Adili, A., Piotrowitz, K., Abdullah, Z., Boege, Y., Stemmer, K., Ringelhan, M., Simonavicius, N., Egger, M., Wohlleber, D., et al. (2014). Metabolic activation of intrahepatic CD8+ T cells and NKT cells causes nonalcoholic steatohepatitis and liver cancer via cross-talk with hepatocytes. Cancer Cell *26*, 549–564.
Wynn, T.A., Chawla, A., and Pollard, J.W. (2013). Macrophage biology in development, homeostasis and disease. Nature *496*, 445–455.
Zahner, S.P., Kel, J.M., Martina, C.A.E., Brouwers-Haspels, I., van Roon, M.A., and Clausen, B.E. (2011). Conditional deletion of TGF-βR1 using Langerin-Cre mice results in Langerhans cell deficiency and reduced contact hypersensitivity. J. Immunol. Baltim. Md 1950 *187*, 5069–5076.
Zeng, Z., Surewaard, B.G.J., Wong, C.H.Y., Geoghegan, J.A., Jenne, C.N., and Kubes, P. (2016). CRIg Functions as a Macrophage Pattern Recognition Receptor to Directly Bind and Capture Blood-Borne Gram-Positive Bacteria. Cell Host Microbe *20*, 99–106.
Zigmond, E., Samia-Grinberg, S., Pasmanik-Chor, M., Brazowski, E., Shibolet, O., Halpern, Z., and Varol, C. (2014). Infiltrating monocyte-derived macrophages and resident kupffer cells display different ontogeny and functions in acute liver injury. J. Immunol. Baltim. Md 1950 *193*, 344–353.

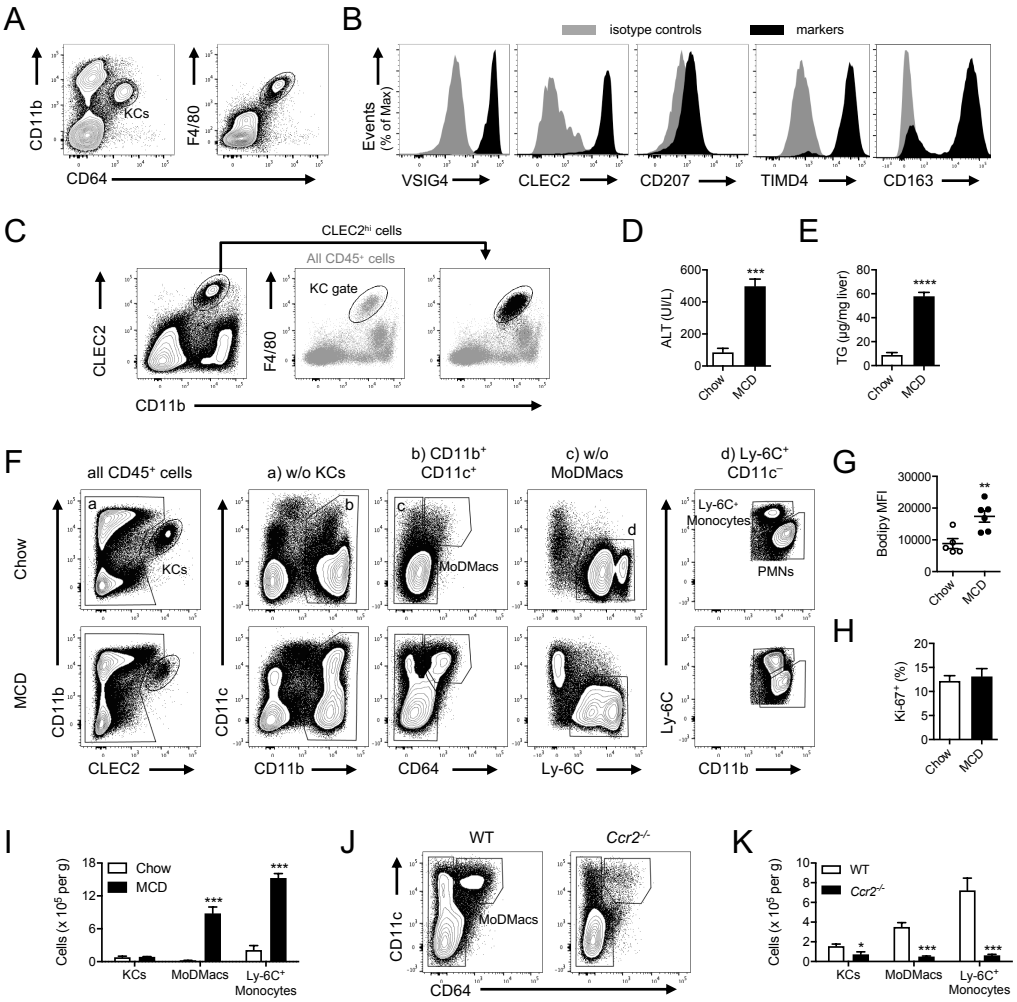
A
CD11b
KCs
CD64
F4/80
B
isotype controls
markers
Events (% of Max)
VSIG4
CLEC2
CD207
TIMD4
CD163
C
CLEC2hi cells
All CD45+ cells
KC gate
CLEC2
F4/80
CD11b
D
ALT (UI/L)
Chow
MCD
E
TG (µg/mg liver)
Chow
MCD
F
all CD45+ cells
a) w/o KCs
b) CD11b+ CD11c+
c) w/o MoDMacs
d) Ly-6C+ CD11c−
Chow
MCD
KCs
MoDMacs
Ly-6C+ Monocytes
PMNs
CD11b
CLEC2
CD11c
CD64
Ly-6C
G
Bodipy MFI
Chow
MCD
H
Ki-67+ (%)
Chow
MCD
I
Cells (x 10^5 per g)
Chow
MCD
KCs
MoDMacs
Ly-6C+ Monocytes
J
WT
Ccr2-/-
CD11c
MoDMacs
CD64
K
Cells (x 10^5 per g)
WT
Ccr2-/-
KCs
MoDMacs
Ly-6C+ Monocytes

Figure 1.

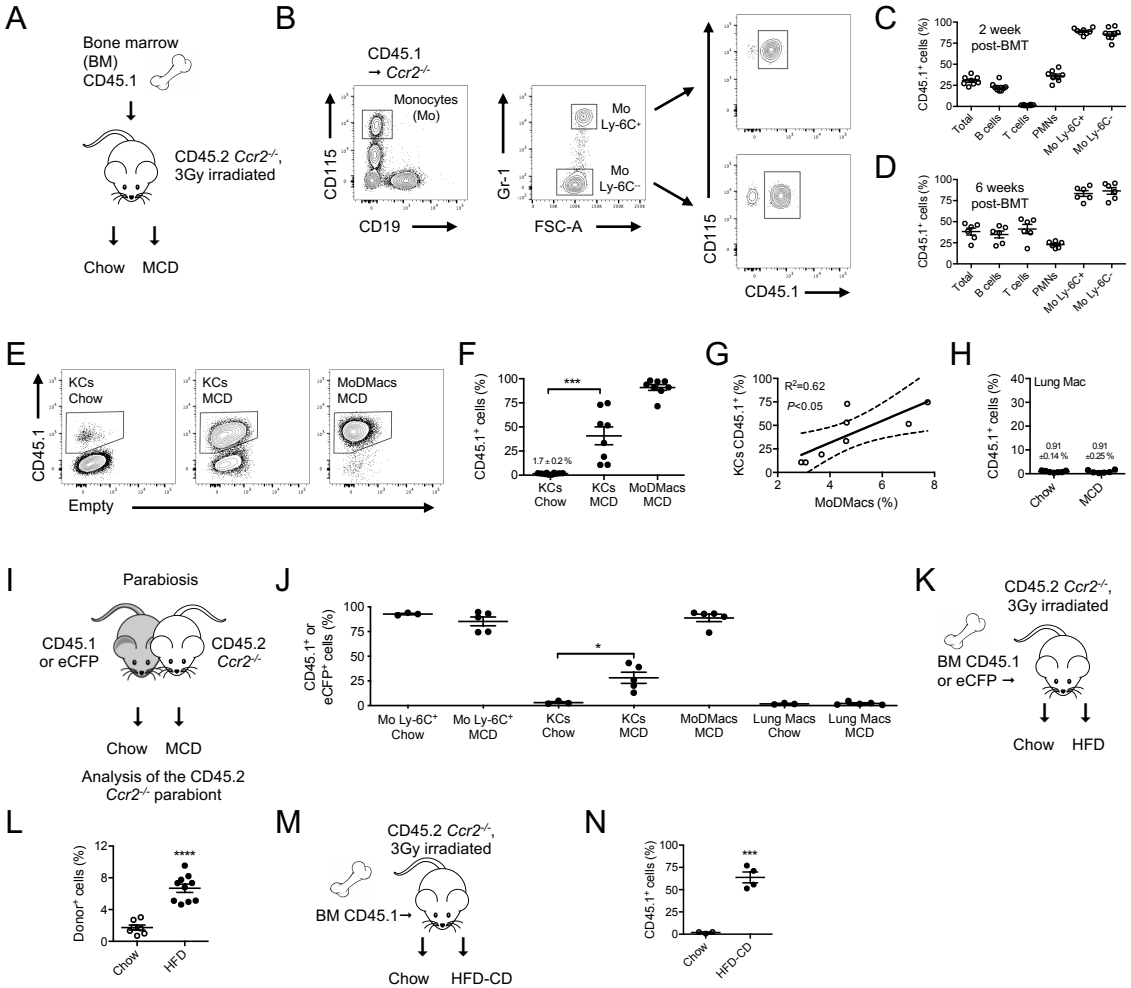
A
Bone marrow (BM) CD45.1
CD45.2 Ccr2-/-, 3Gy irradiated
Chow
MCD
B
CD45.1 → Ccr2-/-
Monocytes (Mo)
CD115
CD19
Gr-1
FSC-A
Mo Ly-6C+
Mo Ly-6C-
CD115
CD45.1
C
2 week post-BMT
CD45.1+ cells (%)
Total
B cells
T cells
PMNs
Mo Ly-6C+
Mo Ly-6C-
D
6 weeks post-BMT
E
KCs Chow
KCs MCD
MoDMacs MCD
CD45.1
Empty
F
***
1.7 ± 0.2 %
KCs Chow
KCs MCD
MoDMacs MCD
G
R2=0.62
P<0.05
KCs CD45.1+ (%)
MoDMacs (%)
H
Lung Mac
0.91 ±0.14 %
0.91 ±0.25 %
Chow
MCD
I
Parabiosis
CD45.1 or eCFP
CD45.2 Ccr2-/-
Chow
MCD
Analysis of the CD45.2 Ccr2-/- parabiont
J
CD45.1+ or eCFP+ cells (%)
*
Mo Ly-6C+ Chow
Mo Ly-6C+ MCD
KCs Chow
KCs MCD
MoDMacs MCD
Lung Macs Chow
Lung Macs MCD
K
CD45.2 Ccr2-/-, 3Gy irradiated
BM CD45.1 or eCFP →
Chow
HFD
L
Donor+ cells (%)
****
Chow
HFD
M
CD45.2 Ccr2-/-, 3Gy irradiated
BM CD45.1→
Chow
HFD-CD
N
CD45.1+ cells (%)
***
Chow
HFD-CD

Figure 2.

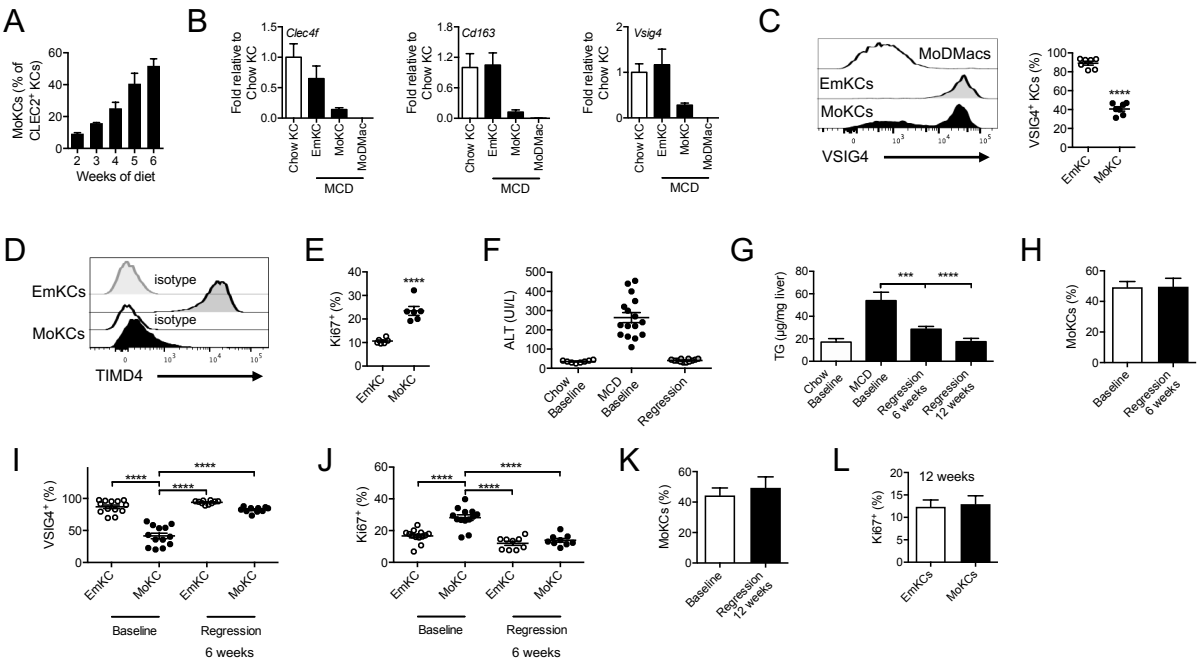
A
MoKCs (% of CLEC2+ KCs)
Weeks of diet
B
Clec4f
Cd163
Vsig4
Fold relative to Chow KC
Chow KC
EmKC
MoKC
MoDMac
MCD
C
MoDMacs
EmKCs
MoKCs
VSIG4
VSIG4+ KCs (%)
D
isotype
TIMD4
E
Ki67+ (%)
F
ALT (UI/L)
Chow Baseline
MCD Baseline
Regression
G
TG (µg/mg liver)
Regression 6 weeks
Regression 12 weeks
H
Baseline
I
VSIG4+ (%)
Regression
6 weeks
J
K
L
12 weeks

Figure 3.

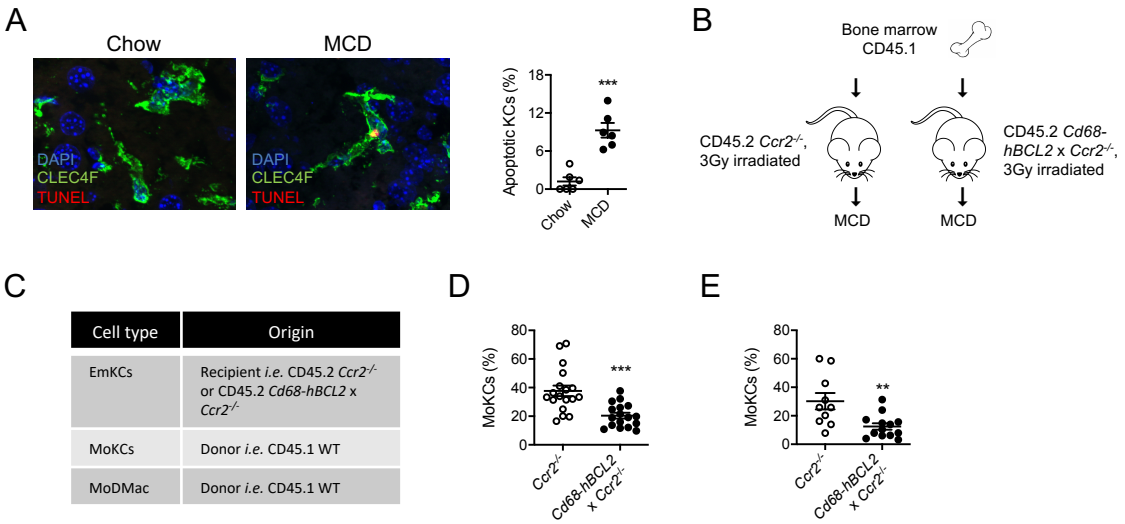
A
Chow
MCD
DAPI
CLEC4F
TUNEL
Apoptotic KCs (%)
18
12
6
0
***
Chow
MCD
B
Bone marrow
CD45.1
CD45.2 Ccr2-/-,
3Gy irradiated
CD45.2 Cd68-
hBCL2 x Ccr2-/-,
3Gy irradiated
MCD
MCD
C
Cell type
Origin
EmKCs
Recipient i.e. CD45.2 Ccr2-/- or CD45.2 Cd68-hBCL2 x Ccr2-/-
MoKCs
Donor i.e. CD45.1 WT
MoDMac
Donor i.e. CD45.1 WT
D
MoKCs (%)
80
60
40
20
0
***
Ccr2-/-
Cd68-hBCL2 x Ccr2-/-
E
MoKCs (%)
80
60
40
20
0
**
Ccr2-/-
Cd68-hBCL2 x Ccr2-/-

Figure 4.

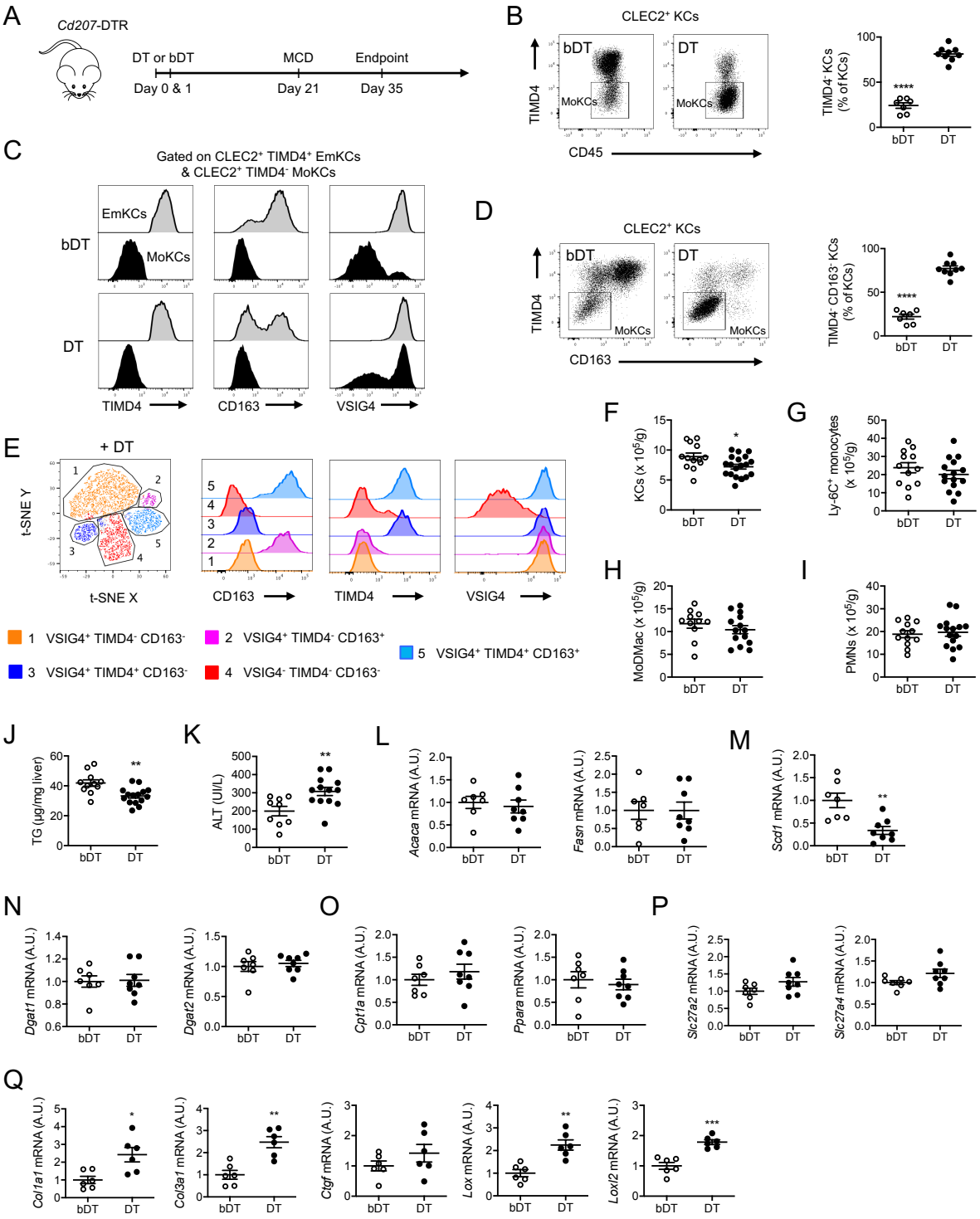
A
Cd207-DTR
DT or bDT
Day 0 & 1
MCD
Day 21
Endpoint
Day 35
B
CLEC2+ KCs
bDT
DT
MoKCs
TIMD4
CD45
TIMD4- KCs (% of KCs)
C
Gated on CLEC2+ TIMD4+ EmKCs & CLEC2+ TIMD4- MoKCs
EmKCs
MoKCs
TIMD4
CD163
VSIG4
D
CLEC2+ KCs
TIMD4- CD163- KCs (% of KCs)
E
+ DT
t-SNE Y
t-SNE X
1 VSIG4+ TIMD4- CD163-
2 VSIG4+ TIMD4- CD163+
3 VSIG4+ TIMD4+ CD163-
4 VSIG4- TIMD4- CD163-
5 VSIG4+ TIMD4+ CD163+
F
KCs (x 10^5/g)
G
Ly-6C+ monocytes (x 10^5/g)
H
MoDMac (x 10^5/g)
I
PMNs (x 10^5/g)
J
TG (µg/mg liver)
K
ALT (UI/L)
L
Acaca mRNA (A.U.)
Fasn mRNA (A.U.)
M
Scd1 mRNA (A.U.)
N
Dgat1 mRNA (A.U.)
Dgat2 mRNA (A.U.)
O
Cpt1a mRNA (A.U.)
Ppara mRNA (A.U.)
P
Slc27a2 mRNA (A.U.)
Slc27a4 mRNA (A.U.)
Q
Col1a1 mRNA (A.U.)
Col3a1 mRNA (A.U.)
Ctgf mRNA (A.U.)
Lox mRNA (A.U.)
Loxl2 mRNA (A.U.)
bDT
DT

Figure 5.

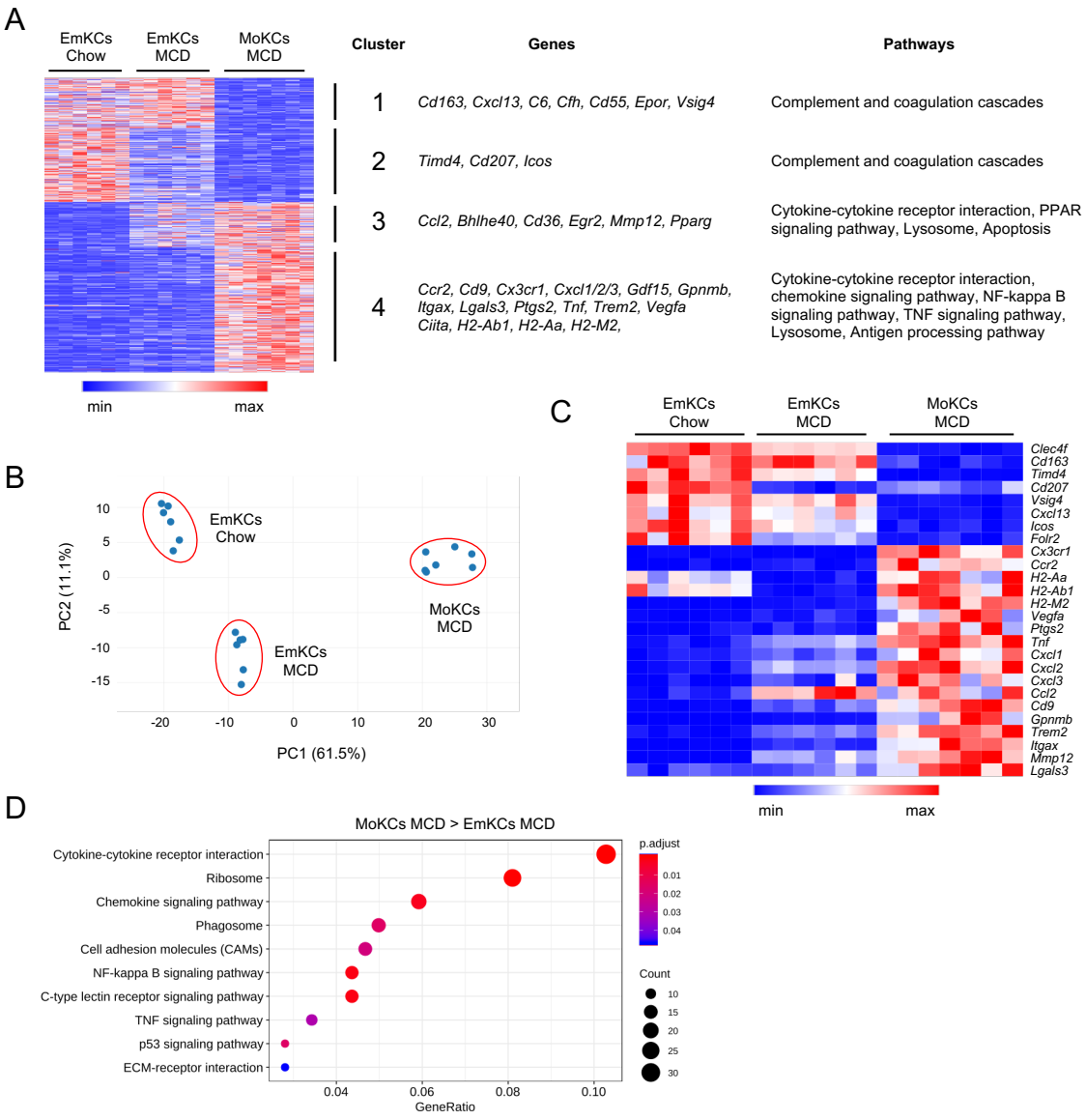
A
EmKCs Chow
EmKCs MCD
MoKCs MCD
Cluster
Genes
Pathways
1
Cd163, Cxcl13, C6, Cfh, Cd55, Epor, Vsig4
Complement and coagulation cascades
2
Timd4, Cd207, Icos
Complement and coagulation cascades
3
Ccl2, Bhlhe40, Cd36, Egr2, Mmp12, Pparg
Cytokine-cytokine receptor interaction, PPAR signaling pathway, Lysosome, Apoptosis
4
Ccr2, Cd9, Cx3cr1, Cxcl1/2/3, Gdf15, Gpnmb, Itgax, Lgals3, Ptgs2, Tnf, Trem2, Vegfa Ciita, H2-Ab1, H2-Aa, H2-M2,
Cytokine-cytokine receptor interaction, chemokine signaling pathway, NF-kappa B signaling pathway, TNF signaling pathway, Lysosome, Antigen processing pathway
min
max
B
EmKCs Chow
MoKCs MCD
EmKCs MCD
PC2 (11.1%)
PC1 (61.5%)
C
EmKCs Chow
EmKCs MCD
MoKCs MCD
Clec4f
Cd163
Timd4
Cd207
Vsig4
Cxcl13
Icos
Folr2
Cx3cr1
Ccr2
H2-Aa
H2-Ab1
H2-M2
Vegfa
Ptgs2
Tnf
Cxcl1
Cxcl2
Cxcl3
Ccl2
Cd9
Gpnmb
Trem2
Itgax
Mmp12
Lgals3
min
max
D
MoKCs MCD > EmKCs MCD
Cytokine-cytokine receptor interaction
Ribosome
Chemokine signaling pathway
Phagosome
Cell adhesion molecules (CAMs)
NF-kappa B signaling pathway
C-type lectin receptor signaling pathway
TNF signaling pathway
p53 signaling pathway
ECM-receptor interaction
GeneRatio
p.adjust
Count

Figure 6.

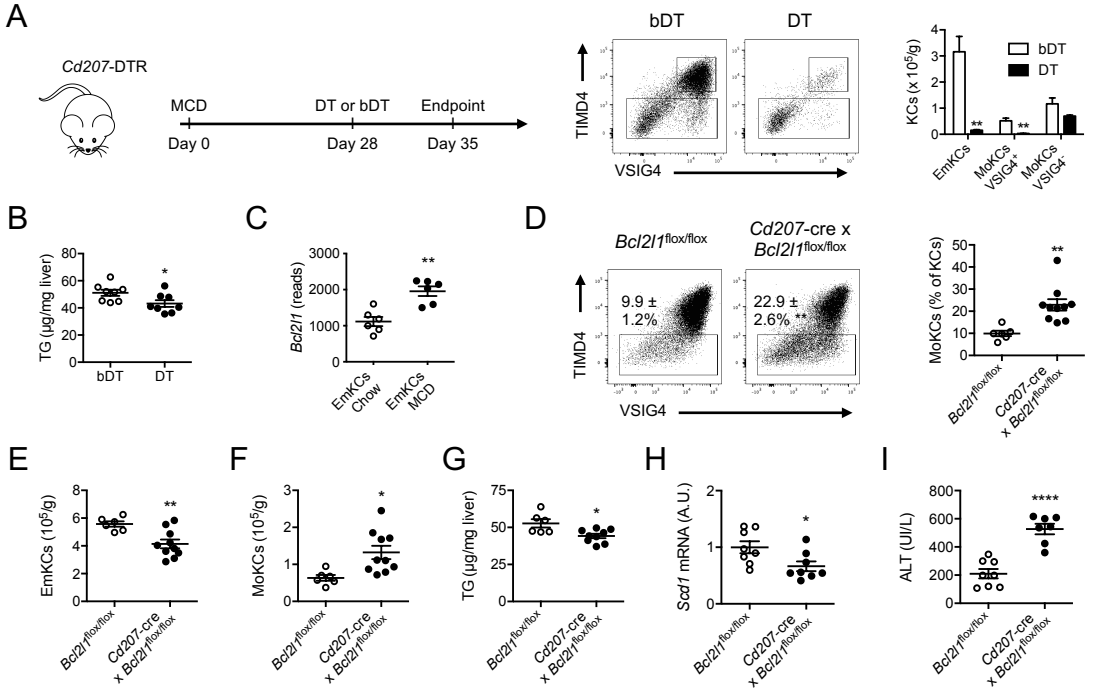
A
Cd207-DTR
MCD
Day 0
DT or bDT
Day 28
Endpoint
Day 35
bDT
DT
TIMD4
VSIG4
KCs (x 10^5/g)
EmKCs
MoKCs VSIG4+
MoKCs VSIG4-
B
TG (µg/mg liver)
C
Bcl2l1 (reads)
EmKCs Chow
EmKCs MCD
D
Bcl2l1flox/flox
Cd207-cre x Bcl2l1flox/flox
9.9 ± 1.2%
22.9 ± 2.6%
MoKCs (% of KCs)
E
EmKCs (10^5/g)
F
MoKCs (10^5/g)
G
TG (µg/mg liver)
H
Scd1 mRNA (A.U.)
I
ALT (UI/L)

Figure 7.